



An energy-relaxation-based framework for the modeling of magnetic shape memory alloys—Simulation of three-dimensional effects under homogeneous loading conditions

Thorsten Bartel^{a,*}, Bjoern Kiefer^b, Andreas Menzel^{a,c}

^a Institute of Mechanics, TU Dortmund, Leonhard-Euler-Str. 5, 44227 Dortmund, Germany

^b Institute of Mechanics and Fluid Dynamics, TU Bergakademie Freiberg, Lampadiusstr. 4, 09599 Freiberg, Germany

^c Division of Solid Mechanics, Lund University, PO Box 118, 22100 Lund, Sweden

ARTICLE INFO

Article history:

Received 25 June 2020

Received in revised form 7 September 2020

Accepted 22 October 2020

Available online 04 November 2020

Keywords:

Magnetic shape memory alloys

Constitutive modeling

Three-dimensional model formulation

Micromechanics

Micromagnetics

Magnetomechanical coupling

ABSTRACT

It is known from experimental findings that three-dimensional effects can have a strong influence on magnetic shape memory behavior. Such phenomena are, however, often neglected in MSMA constitutive models, as they only become meaningful under complex loading conditions. The extensions of our original modeling framework, cf. Bartel et al. (2020), to include 3D-effects is threefold: (i) vector-valued microstructural variables are now elements in \mathbb{R}^3 , i.e. no longer parameterizable in polar coordinates, (ii) a third tetragonal martensite variant may form/vanish by switching from/back into both other variants, and (iii) a more general and robust algorithmic treatment is necessary. The latter includes the implementation of a staggered Augmented Lagrangian scheme to handle the now much larger and numerically more advanced sets of equality and inequality constraints. In this context, two extended model formulations are presented. The first considers a first-order, two-variant laminate approach (rank-one convexification), in which domain magnetizations, interface orientations etc. are now three-dimensional vectors. The second model is based on a convexification approach, for which the incorporation of the third martensitic variant is quite natural. Numerical examples are investigated to test the generalized modeling framework. Firstly, it is confirmed that both extended models recover the solution of the previously established two-dimensional model for a simple loading case. Secondly, response predictions for more complex loading scenarios (non-proportional bi-axial stresses, orthogonal magnetic field), motivated by experiments, are investigated. It is found that capturing the formation, elimination and mutual interaction of all martensitic variants as well as general three-dimensional magnetization vector orientations is of key importance under these conditions. The extended convexification model and modified algorithmic formulation are shown to reliably handle even such general cases.

© 2020 Elsevier Ltd. All rights reserved.

1. Introduction

The authors recently established an energy relaxation-based modeling framework for magnetic shape memory behavior that captures all of the central MSMA response characteristics under complex magnetomechanical loading (Kiefer et al., 2015; Bartel et al., 2020). Moreover, a mixed finite-element formulation was proposed in Buckmann et al. (2019) that is capable of accommodating the implementation of this type of constitutive model, globally enforcing physical inequality constraints on evolving microstructural variables and properly handling inhomogeneous

demagnetization fields and remotely applied magnetic boundary conditions. This notwithstanding, the motivation for the present work is that pronounced three-dimensional effects in MSMA behavior—which are not yet captured by that modeling and simulation framework—can come into play for a number of reasons. Due to the dependence of the effective response on the sample shape (demagnetization effect), the magnetostatic boundary-value problem is nearly always three-dimensional. This is typically handled through appropriate shape factors. A more subtle aspect appears when considering local effects, in that corners of non-ellipsoidal samples experience three-dimensionally oriented fields, even if the external loading direction is restricted to a specific plane or even to one of the coordinate axes. The higher the complexity of the loading scenario—or even for simple scenarios with misalignment between load application and characteristic directions (e.g.

* Corresponding author.

E-mail address: thorsten.bartel@udo.edu (T. Bartel).

crystal orientation, easy axes etc.)—will generally trigger more complex microstructural arrangements. These can simultaneously include all martensitic variants of the corresponding symmetry group.

Detailed overviews regarding the literature on MSMA modeling have been presented by the authors in Kiefer and Lagoudas (2005), Kiefer and Lagoudas (2008), Kiefer and Lagoudas (2009) and Kiefer et al. (2015). See also Kiang and Tong (2005) for a review of some earlier model developments. In recent years, different groups have proposed first constitutive models for three-dimensional MSMA behavior, for instance (Kiang and Tong, 2007; Gauthier et al., 2011; Chen et al., 2014; LaMaster et al., 2015; Auricchio et al., 2015; Feigenbaum et al., 2016). These models address different aspects of three-dimensionality (3D vector parameterizations, 3D magnetostatic boundary value problems, three-variant formulations), but usually not all of them.

Only very few works have approached the modeling of MSMA response through the notion of *energy relaxation*. Mathematically, this concept builds on interpreting the loss of quasiconvexity (Morrey, 1952), or approximations thereof, as a material instability that leads to the formation of microstructure. Practically speaking, it is checked—for the purely mechanical case—whether the perturbation of a homogeneous deformation state lowers the energy of the system. Another way of describing this approach is that each phase in a phase-transforming solid material is associated with a preferred strain state, which represents a local minimum in a non-convex (multi-well) energy landscape. The relaxed energy—which allows the decomposition of the material into individual phases, if this helps to lower the energy—then describes the stable effective behavior of the phase mixture in form of the quasi-convex energy hull. If these perturbations are not completely general, but rather of laminate type with strain compatible interfaces, the approach is termed rank-one convexification, which yields an upper bound to the quasi-convex envelope. For a more formal introduction, the reader is also referred to Bartel et al. (2020). With the aim of introducing magnetomechanical coupling in this context, DeSimone and James (2002) established the constrained theory of magnetoelasticity, which combines the Ball and James (1987) theory on martensitic microstructures as minimizers of energy with elements of micromagnetics theory, see Brown (1963, 1966) and DeSimone et al. (2006). Applications of the constrained theory to MSMA modeling were discussed in Tickle et al. (1999), DeSimone and James (2002), DeSimone (2004) and Kiefer et al. (2015). Moreover, Ma and Li (2007) and Li and Ma (2008) proposed a higher-order laminate model for MSMA. Note that these

approaches typically neglect dissipative effects. A concise review of the energy relaxation modeling framework previously established by the authors is presented in Section 2.

The paper is structured as follows: The mentioned review of our prior work in Section 2 is meant to set the stage for the subsequent development of the model extensions that account for various three-dimensional phenomena, beginning with Section 3. A detailed discussion of the algorithmic treatment of the model equations—nonlinear minimization problems with nonlinear (in-) equality constraints—is given in Section 4. Representative numerical examples, including a verification test, are presented in Section 5. The paper concludes with a summary of the novel contributions and an outlook on on-going and future work in Section 6.

2. Review of the original modeling framework

The continuum thermodynamics-based models for magnetic shape memory behavior developed by Kiefer and Lagoudas were essentially built in the tradition of constitutive models for conventional thermal SMA (Kiefer and Lagoudas, 2005; Lagoudas, 2008; Kiefer and Lagoudas, 2009; Kiefer et al., 2012). These, in turn, bear great resemblance to classical plasticity models. In recent years, however, a fundamentally different approach was taken by the authors to model MSMA, in following the concepts of energy relaxation which have already been successfully established to model the behavior of SMA (Bartel and Hackl, 2009; Bartel et al., 2011; Bartel et al., 2015). In order to clearly point out the novel aspects of the current contribution, a brief review of a previously established energy relaxation model for MSMA shall be given here.

The unique response characteristics of MSMA are directly related to the evolution of *microstructure*. In this context, the term microstructure relates to mixtures of crystallographic variants and magnetization orientations (domains) in the ferromagnetic martensite phase, see Fig. 1. For the magnetic shape memory effect—the magnetic field-induced martensite reorientation—to occur, the material needs to simultaneously possess low twinning stress (resistance to twin boundary motion/variant switching) and high magnetocrystalline anisotropy (resistance to rotation of magnetic moments away from easy axes). The relaxation modeling approach then builds on the computation of a set of energy-minimizing microstructural variables, based on a canonical variational principle, for each instance in the loading history. The specific model proposed in Bartel et al. (2020)—cf. also the earlier

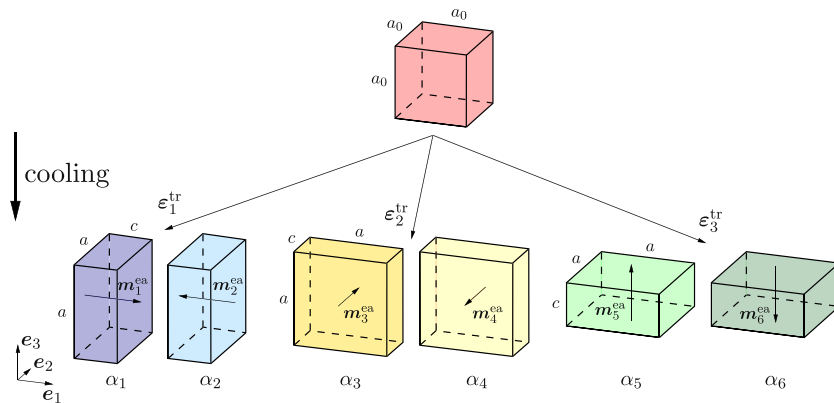


Fig. 1. Illustration of crystallographic variants and domain types. Below both the Curie and the phase transformation temperatures, typical MSMA consist of ferromagnetic martensites, here schematically shown in the (5 M) tetragonal structure occurring in Ni₂MnGa (Heczko et al., 2003). The variants that arise due to the lower symmetry of this phase—compared to the cubic austenite parent phase—are distinguishable by their respective transformation strains. While the easy axis of each variant is always along the short edge of the unit cell, the sense of direction (positive or negative) of the spontaneous magnetization can be used to further distinguish different domain types. Consequently, a total of six variant/domain combinations, with volume fractions $\alpha_1, \dots, \alpha_6$, can be identified in this case. Figure taken from Bartel et al. (2020).

Table 1

Summary of the original two-dimensional, two variant modeling framework proposed in Bartel et al. (2020). For the sake of brevity, all superscripts indicating that all time-dependent variables are to be evaluated at t_{n+1} have been neglected.

1. Incremental canonical constitutive minimization principle:

$$\mathbf{p} = \arg \min_{\mathbf{p} \in \mathcal{A}} \{ \Pi_{\text{hom}}^{\text{rel}}(\mathbf{p}) + \mathfrak{D}(\mathbf{p}, {}^n\mathbf{p}) \} \quad (1)$$

with

$$\mathcal{A} = \{ 0 \leq \xi_1 \leq 1, |\eta_1| \leq \xi_1, |\eta_2| \leq 1 - \xi_1, |\theta_1| \leq \pi/2, |\theta_3| \leq \pi/2 \}. \quad (2)$$

2. Reduced set of microstructural variables:

$$\mathbf{p} = \{ \xi_1, \eta_1, \eta_2, \theta_1, \theta_3, \varphi \} \quad (\text{with: } \xi_2 = [1 - \xi_1], \theta_2 = -\theta_1, \theta_4 = -\theta_3) \quad (3)$$

3. Relation of average strains and magnetizations to microstructural variables (see Fig. 1):

$$\boldsymbol{\varepsilon}(\mathbf{p}) = \mathbf{E}^{-1} : \bar{\boldsymbol{\sigma}} + \boldsymbol{\varepsilon}^{\text{tr}}, \quad \text{with } \boldsymbol{\varepsilon}^{\text{tr}} = \xi_1 \boldsymbol{\varepsilon}_1^{\text{tr}} + [1 - \xi_1] \boldsymbol{\varepsilon}_2^{\text{tr}}, \quad (4)$$

$$\mathbf{m}(\mathbf{p}) = \sum_{j=1}^4 \alpha_j \mathbf{m}_j^{\text{dom}}(\theta_j), \quad \text{where } \alpha_{2i-1} = \frac{1}{2} [\xi_i + \eta_i], \alpha_{2i} = \frac{1}{2} [\xi_i - \eta_i], \quad \text{for } i = 1, 2, \quad (5)$$

and domain magnetizations

$$\begin{aligned} \mathbf{m}_1^{\text{dom}}(\theta_1) &= m_s [\cos(\theta_1) \mathbf{e}_1 + \sin(\theta_1) \mathbf{e}_2], & \mathbf{m}_2^{\text{dom}}(\theta_2) &= -m_s [\cos(\theta_2) \mathbf{e}_1 + \sin(\theta_2) \mathbf{e}_2], \\ \mathbf{m}_3^{\text{dom}}(\theta_3) &= m_s [-\sin(\theta_3) \mathbf{e}_1 + \cos(\theta_3) \mathbf{e}_2], & \mathbf{m}_4^{\text{dom}}(\theta_4) &= m_s [\sin(\theta_4) \mathbf{e}_1 - \cos(\theta_4) \mathbf{e}_2]. \end{aligned} \quad (6)$$

4. Partially-relaxed incremental energy storage functional:

$$\Pi_{\text{hom}}^{\text{rel}}(\mathbf{p}) = \left[R_1 \psi(\mathbf{p}) + \frac{\mu_0}{2} \mathbf{m}(\mathbf{p}) \cdot \mathbf{D} \cdot \mathbf{m}(\mathbf{p}) - \mu_0 \bar{\mathbf{h}} \cdot \mathbf{m}(\mathbf{p}) - \bar{\boldsymbol{\sigma}} : \boldsymbol{\varepsilon}(\mathbf{p}) \right] V_{\mathcal{A}}. \quad (7)$$

5. Free energy density of the phase mixture:duced set of microstructural variable

$$\psi = \sum_{i=1}^2 \left[\xi_i \psi_i^{\text{el}} + \sum_{j=2i-1}^{2i} \alpha_j \psi_j^{\text{ani}} \right]. \quad (8)$$

6. Elastic and magnetocrystalline anisotropy contributions:

$$\psi_i^{\text{el}} = \frac{1}{2} \boldsymbol{\varepsilon}_i^{\text{el}} : \mathbf{E}_i : \boldsymbol{\varepsilon}_i^{\text{el}}, \quad \psi_j^{\text{ani}} = K \sin^2(\theta_j), \quad (9)$$

with the elastic phase strains

$$\boldsymbol{\varepsilon}_1^{\text{el}} = \boldsymbol{\varepsilon} + \xi_2 [\mathbf{a} \otimes \hat{\mathbf{n}}_{12}^{\text{tw}}]^{\text{sym}} - \boldsymbol{\varepsilon}_1^{\text{tr}}, \quad \boldsymbol{\varepsilon}_2^{\text{el}} = \boldsymbol{\varepsilon} - \xi_1 [\mathbf{a} \otimes \hat{\mathbf{n}}_{12}^{\text{tw}}]^{\text{sym}} - \boldsymbol{\varepsilon}_2^{\text{tr}}, \quad (10)$$

and the twin boundary orientation

$$\hat{\mathbf{n}}_{12}^{\text{tw}} = \cos(\varphi) \mathbf{e}_1 + \sin(\varphi) \mathbf{e}_2. \quad (11)$$

7. Relaxed (rank-one convexified) free energy density:

$$R_1 \psi = \inf_{\mathbf{a}} \{ \psi \} = \psi_{\mathbf{a}=\mathbf{a}^*}, \quad (12)$$

with (analytical) optimal strain jump

$$\mathbf{a}^* = \arg \inf_{\mathbf{a}} \{ \psi \} = -[\hat{\mathbf{n}}_{12}^{\text{tw}} \cdot \mathbf{E} \cdot \hat{\mathbf{n}}_{12}^{\text{tw}}]^{-1} \cdot [\hat{\mathbf{n}}_{12}^{\text{tw}} \cdot \mathbf{E} : [\boldsymbol{\varepsilon}_2^{\text{tr}} - \boldsymbol{\varepsilon}_1^{\text{tr}}]]. \quad (13)$$

8. Incremental dissipation functional

$$\mathfrak{D}(\mathbf{p}, {}^n\mathbf{p}) = [\mathbf{Y}_{\xi_1}(\xi_1) | \xi_1 - {}^n\xi_1 | + \mathbf{Y}_{\varphi} | \varphi - {}^n\varphi |] V_{\mathcal{A}}. \quad (14)$$

with hardening-type switching limit

$$\mathbf{Y}_{\xi}(\xi_1) = \begin{cases} \mathbf{Y}_{\xi}^0 + \xi_1 \Delta \mathbf{Y}_{\xi}, & \text{if } \xi_1 > {}^n\xi_1 \\ \mathbf{Y}_{\xi}^0 + [1 - \xi_1] \Delta \mathbf{Y}_{\xi}, & \text{if } \xi_1 < {}^n\xi_1 \end{cases} \quad (15)$$

version described in Kiefer et al. (2015)—is summarized in Table 1. Note that inelastic (hysteretic) effects are incorporated by working with a rate-type (time-incremental) minimization principle, in the sense of a standard dissipative material (Biot, 1965; Halphen and Nguyen, 1975; Miehe et al., 2011). All of the main model ingredients listed in Table 1 will be discussed in Section 3, in the context of its generalization.

In addition to the general constitutive relations specified in Table 1, specific forms (symmetries) must still be selected for the elasticity, transformation strain, and demagnetization tensors, which are considered to be input to the model. Common choices are:

$$\begin{aligned} \mathbf{E} &= \left[\frac{\nu E}{[1 + \nu][1 - 2\nu]} \delta_{ij} \delta_{kl} + \frac{E}{2[1 + \nu]} [\delta_{ik} \delta_{jl} + \delta_{il} \delta_{jk}] \right] \mathbf{e}_i \otimes \mathbf{e}_j \\ &\otimes \mathbf{e}_k \otimes \mathbf{e}_l, \end{aligned} \quad (16)$$

which corresponds to assuming elastic isotropy (for the sake of simplicity),

$$\begin{aligned} \boldsymbol{\varepsilon}_1^{\text{tr}} &= b_2 \mathbf{e}_1 \otimes \mathbf{e}_1 + b_1 [\mathbf{e}_2 \otimes \mathbf{e}_2 + \mathbf{e}_3 \otimes \mathbf{e}_3], \\ \boldsymbol{\varepsilon}_2^{\text{tr}} &= b_2 \mathbf{e}_2 \otimes \mathbf{e}_2 + b_1 [\mathbf{e}_1 \otimes \mathbf{e}_1 + \mathbf{e}_3 \otimes \mathbf{e}_3], \end{aligned} \quad (17)$$

to describe the Bain strains of a cubic to (nearly) tetragonal martensitic transformation, and

$$\mathbf{D} = D_{11} \mathbf{e}_1 \otimes \mathbf{e}_1 + \frac{1 - D_{11}}{2} [\mathbf{e}_2 \otimes \mathbf{e}_2 + \mathbf{e}_3 \otimes \mathbf{e}_3], \quad \text{so that} \quad \text{tr} \mathbf{D} = 1, \quad (18)$$

as shape factor for a prismatic sample geometry, with a symmetric cross-section normal to the x_1 -direction and x_2, x_3 principal axes. Note that the demagnetization factors can either be taken from tables available in the literature for simple geometries (O'Handley, 2000) or computed beforehand, e.g. via finite element analysis of the magnetostatic boundary value problem. For non-ellipsoidal geometries, with inhomogeneous demagnetization fields, these shape factors are volume averages—and their use in the context of inhomogeneous magnetization fields must be treated with care. For a more detailed discussion of this point, see Haldar et al. (2011) and Buckmann et al. (2019).

There are several distinct advantages to this modeling approach. Both the underlying parameter set—which is surprisingly small with nine material and two shape parameters, considering the complexity of the predicted response—and the microstructural variables consist of physically well-motivated and easily interpretable quantities. Moreover, all key mechanisms (variant switching, domain wall motion, magnetization rotation) may occur simultaneously and in arbitrary combinations or order. The model obeys a single physical principle, i.e. stationarity of an energy functional, with no need for purely phenomenological evolution equations. The microstructure formation at each material point is influenced by the magnetostatic energy stored in the entire self-field. Although not explicitly demonstrated here, the approach is strongly rooted in mathematical analysis, related to the existence of minimizers for the underlying variational problems (i.e. direct methods in the calculus of variations), see, e.g., Dacorogna (1982). Most importantly perhaps, the model captures all of the key response features characteristic of single crystalline MSMA behavior (e.g. nonlinear, anisotropic, stress-level and loading history-dependent magnetic field-induced strain and magnetization responses, magnetic field-biased pseudoelasticity etc.) and its predictions have been validated by experiments—where relevant data was available. A small caveat to the current formulation is that no effort has been made to enforce magnetic compatibility at the twin and domain interfaces. Nevertheless, effective magnetization response curves predicted by this approach seem to already be quite accurate (cf. Bartel et al., 2020). Pairwise compatibility is (trivially) satisfied in the tetragonal martensite with uniaxial magnetocrystalline symmetry, if magnetization vectors are assumed to be fixed to their respective easy axes. For the general case, however, this may not be true. It is, in fact, still an open question whether or not the strict enforcement of magnetic compatibility is even sensible, since this may lead to overly constrained problems. There are also indications that in reality more complex domain structures form near such interfaces to achieve compatibility. DeSimone and James (2002) further state that it may be necessary to include excess magnetostatic energy terms to accurately describe this situation. While this debate is left to future work, first ideas of including notions of magnetic interface compatibility in energy relaxation models have recently been discussed in Kiefer and Bartel (2017).

The central motivation for the work presented in this paper is that the model summarized in Table 1 only permits stress $\bar{\sigma}(t)$ and magnetic field $\bar{\mathbf{h}}(t)$ loads limited to the x_1 - x_2 -plane. The reason is the restriction of the formulation to a two-variant setting, with the microstructure-defining quantities parameterized in only two dimensions. This is not necessarily always a severe limitation—e.g. for typical simple MSMA testing setups (Kiefer et al., 2007)—but certainly if more complex loading scenarios are to be considered, as for example discussed in Feigenbaum et al. (2016). One must also be mindful that even one-dimensional magnetic

loading already leads to three-dimensional magnetic fields, and therefore magnetization fields, in non-ellipsoidal samples—although this effect is typically limited to small regions in simple geometries. Section 3 discusses the natural—yet quite challenging—extensions that have been made to the framework presented in this section, to account for three-dimensional effects in MSMA behavior.

3. Extended constitutive models

Having discussed the general energy relaxation framework for MSMA modeling in the previous section, two extended constitutive models shall now be introduced. The focus of these generalizations is to capture the described additional effects characteristic of MSMA behavior under fully three-dimensional loading conditions.

3.1. Model I: laminate approach

The first extended model presented here—the (first-order) laminate approach—shares many similarities with the original model previously summarized in Table 1. In particular, the two-variant setting is maintained. The extension consists of the following aspects:

- (i) The elastic anisotropy of each martensite variant is generally considered in terms of different elasticity tensors—or, more precisely, different orientations of the same tensor. As a consequence, expression (4) is no longer valid.
- (ii) In view of point (i) and further model modifications, it may not be possible—or at least quite cumbersome—to still find analytical solutions for the strain jump across the laminate interface, vector \mathbf{a} , cf. (13). Therefore, this quantity is now individually incorporated as an independent state variable, in terms of its Cartesian coordinates a_i .
- (iii) In the two-dimensional setting, it was possible to parameterize the laminate orientation vector \mathbf{n}^{tw} via the angle φ representing the rotation of the twin interface in the x_1 - x_2 -plane, cf. (3). As another step towards a fully three-dimensional formulation, $\mathbf{n}^{\text{tw}} \in \mathcal{S}^2$ is now considered, where \mathcal{S}^{d-1} denotes the unit hyper-sphere in \mathbb{R}^d . Instead of relying on spherical coordinates—potentially exhibiting well-known singularity issues—the vector $\mathbf{n}^{\text{tw}} = n_i^{\text{tw}} \mathbf{e}_i \in \mathbb{R}^3$ is parameterized by its three Cartesian coordinates n_i^{tw} and the constraint $\|\mathbf{n}^{\text{tw}}\| = 1$ is additionally enforced. Please note, that enforcing compatibility w.r.t. the Bain strains would yield analytical solutions for the laminate orientation. In the present case, however, compatibility is considered w.r.t. the total strains so that the laminate orientation also depends on elastic strain contributions. Therefore, such analytical solutions may not exist in general. The reader is referred to Bartel et al. (2020), Section 4.2, and Kiefer et al. (2015), page 176, for related discussions concerning this matter.
- (iv) Following the same line of argumentation, the local magnetization vectors in each domain represented by $\mathbf{m}_j^{\text{dom}}$ are no longer parameterized by the individual rotation angles θ_j , cf. (3) and (6). Instead, analogous to \mathbf{n}^{tw} , their Cartesian coordinates are used along with $\|\mathbf{m}_j^{\text{dom}}\| = m_s$, so that $m_s^{-1} \mathbf{m}_j^{\text{dom}} \in \mathcal{S}^2$.

In comparison to the relations of the original model provided in Table 1, these aspects result in the following model modifications. Regarding extension (i), the total average strain expression accounting for elastic anisotropy takes the form

$$\boldsymbol{\varepsilon}(\mathbf{p}^l) = \mathbf{C} : \left[\bar{\boldsymbol{\sigma}} - \xi_1 [1 - \xi_1] [\mathbf{E}_1 - \mathbf{E}_2] : [\mathbf{a} \otimes \mathbf{n}^{\text{tw}}]^{\text{sym}} + \xi_1 \mathbf{E}_1 : \mathbf{e}_1^{\text{tr}} + [1 - \xi_1] \mathbf{E}_2 : \mathbf{e}_2^{\text{tr}} \right], \quad (19)$$

which replaces (4), with

$$\mathbf{C} := [\xi_1 \mathbf{E}_1 + [1 - \xi_1] \mathbf{E}_2]^{-1} \quad (20)$$

as average compliance tensor of the phase mixture. It is remarked that this, in comparison to (4), more complicated relation purely stems from the assumption of elastic anisotropy. Generalizations (ii)–(iv) further result in the following extended set of microstructural state variables for model I

$$\mathbf{p}^l = \{\xi_1, \eta_1, \eta_2, \mathbf{a}, \mathbf{n}^{\text{tw}}, \mathbf{m}_1^{\text{dom}}, \dots, \mathbf{m}_4^{\text{dom}}\}. \quad (21)$$

Note further that the direct use of the vectors \mathbf{n}^{tw} and $\mathbf{m}_1^{\text{dom}}, \dots, \mathbf{m}_4^{\text{dom}}$ as microstructural state variables renders relations (6) and (11) obsolete. Moreover, in light of (ii), a partial relaxation step—see (12) and (13)—is omitted and the computation of \mathbf{a} directly incorporated into the incremental constitutive minimization principle

$$\mathbf{p} = \arg \min_{\mathbf{p} \in \mathcal{A}} \{\Pi_{\text{hom}}(\mathbf{p}) + \mathfrak{D}(\mathbf{p}, {}^n\mathbf{p})\}. \quad (22)$$

Here, all superscripts indicating evaluation at t_{n+1} have been neglected in order to keep the notation concise. The set \mathcal{A} of equality and inequality constraints to be taken into account in this model is given by

$$\begin{aligned} r_1^l &:= -\xi_1 \leq 0, & r_2^l &:= \xi_1 - 1 \leq 0, \\ r_3^l &:= |\eta_1| - \xi_1 \leq 0, & r_4^l &:= |\eta_2| - [1 - \xi_1] \leq 0, \\ r_5^l &:= \|\mathbf{n}^{\text{tw}}\| - 1 = 0, \\ r_{j+5}^l &:= \|\mathbf{m}_j^{\text{dom}}\| - m_s = 0, \quad j = 1, \dots, 4. \end{aligned} \quad (23)$$

Note that in (22), $\Pi_{\text{hom}}^{\text{el}}(\mathbf{p})$ was replaced by $\Pi_{\text{hom}}(\mathbf{p})$, since its relaxation is now conducted as part of the simultaneous minimization with respect to all microstructural variables. This, in turn, corresponds to using $\psi(\mathbf{p})$, instead of the rank-one convex hull $R_1\psi(\mathbf{p})$, in the incremental energy storage functional expression

$$\Pi_{\text{hom}}(\mathbf{p}) = \left[\psi(\mathbf{p}) + \frac{\mu_0}{2} \mathbf{m}(\mathbf{p}) \cdot \mathbf{D} \cdot \mathbf{m}(\mathbf{p}) - \mu_0 \bar{\mathbf{h}} \cdot \mathbf{m}(\mathbf{p}) - \bar{\boldsymbol{\sigma}} : \boldsymbol{\varepsilon}(\mathbf{p}) \right] V_{\mathcal{B}}. \quad (24)$$

Then, in addition to (19), the free energy density of the phase mixture (8) is modified in that the magnetocrystalline anisotropy energy density contribution assumes the generalized single-constant, uniaxial symmetry form

$$\psi_j^{\text{ani}} = K \left[1 - \left[\frac{1}{m_s} \mathbf{m}_j^{\text{dom}} \cdot \mathbf{n}_j^{\text{ea}} \right]^2 \right], \quad \text{with } j = 1, \dots, 4, \quad (25)$$

where the \mathbf{n}_j^{ea} reflect the easy axis orientation and directionality in each domain type j , which are specifically given by

$$\mathbf{n}_1^{\text{ea}} = \mathbf{e}_1, \quad \mathbf{n}_2^{\text{ea}} = -\mathbf{e}_1, \quad \mathbf{n}_3^{\text{ea}} = \mathbf{e}_2, \quad \mathbf{n}_4^{\text{ea}} = -\mathbf{e}_2 \quad (26)$$

in reference to a Cartesian coordinate frame that is aligned with the single crystal axes, cf. Fig. 1. Clearly, (25) degenerates to (9) in the two-dimensional setting.

Concerning the incremental dissipation functional, two aspects need to be addressed in the extension: Firstly, in view of the subsequent incorporation of a third tetragonal martensite variant in model II, we choose to already represent the contribution related to the irreversible evolution of the variant volume fractions more generally as

$$\mathfrak{D}_{\xi}^t := V_{\mathcal{B}} \int_0^t \left[\frac{Y_{\xi}}{\sqrt{2}} \sqrt{\xi_1^2 + \xi_2^2} \right] d\tau. \quad (27)$$

For the two-variant case considered here, where $\xi_2 = 1 - \xi_1$ and thus $\xi_2 = -\xi_1$, this reduces to

$$\mathfrak{D}_{\xi}^t = V_{\mathcal{B}} \int_0^t \left[\frac{Y_{\xi}}{\sqrt{2}} \sqrt{2\xi_1^2} \right] d\tau = V_{\mathcal{B}} \int_0^t Y_{\xi} |\xi_1| d\tau, \quad (28)$$

which is identical to (14), in the time-discretized description. Secondly, due to the fact that the laminate orientation vector \mathbf{n}^{tw} is parameterized differently compared to the original model, the related term in the dissipation functional is now defined as

$$\mathfrak{D}_{\mathbf{n}}^t := V_{\mathcal{B}} \int_0^t Y_{\mathbf{n}} \|\dot{\mathbf{n}}^{\text{tw}}\| d\tau, \quad (29)$$

The time-discretized form of the total dissipation functional consequently reads

$$\mathfrak{D} := \mathfrak{D}^{t_{n+1}} - \mathfrak{D}^{t_n} \approx [Y_{\xi} |\xi_1 - {}^n\xi_1| + Y_{\mathbf{n}} \|\mathbf{n}^{\text{tw}} - {}^n\mathbf{n}^{\text{tw}}\|] V_{\mathcal{B}}. \quad (30)$$

Note that this function approximates the integrals in (28) and (29) based on $\dot{\mathbf{p}} \approx [\mathbf{p}^{t_{n+1}} - \mathbf{p}^{t_n}]/\Delta t$, defining a constant rate of the (relevant) internal microstructural variables within the time interval $[t_n, t_{n+1}]$, such that $\int_{t_n}^{t_{n+1}} \phi(\dot{\mathbf{p}}) d\tau \approx \Delta t \phi([\mathbf{p}^{t_{n+1}} - \mathbf{p}^{t_n}]/\Delta t)$, where ϕ is supposed to be a generalized function here. Moreover, the threshold value $Y_{\xi} = \hat{Y}_{\xi}(\kappa)$ implicitly depends on the variant volume fractions, in order to describe a hardening-like effect during variant switching, as equivalently done in the original model. In view of the later extension to three martensite variants, the quantity κ has been introduced, which measures the accumulated amount of variant reorientation. The precise treatment of κ is discussed in Section 4.2.

3.2. Model II: convexification approach

Unlike the laminate model, the alternative formulation provided here—the convexification approach—does not allow addressing aspects of strain compatibility or interface orientation at the boundary between neighboring phases. This approach, however, makes the extension to a fully three-dimensional setting much more straightforward, so that all three variants occurring in the tetragonal 5 M martensite of Ni_2MnGa —our material of interest—can now be incorporated into the constitutive model. This feature represents a key extension compared to the original model, as well as to the two-variant laminate formulation. In summary, the main aspects of this generalized modeling framework are:

- (i) Elastic anisotropy is generally included by considering different elasticity tensors for each martensitic variant (as in the laminate model).
- (ii) The magnetization vectors in each domain are parameterized via Cartesian coordinates, together with the respective equality constraints enforcing their fixed length (as in the laminate model).
- (iii) A third tetragonal variant is included in the formulation. The generalization of the framework—regarding all aspects of the extension in model II—is such that it could potentially incorporate more variants, which would be important for materials with other symmetry classes.

Due to the fact that the concept of convexification is quite established and has been applied, for instance, to the modeling of martensitic phase transformations in conventional shape memory alloys (e.g. Junker and Hackl (2011)) or to model the phase transitions during selective laser melting (Bartel et al. (2019)), its key aspects shall briefly be outlined in what follows.

The basic idea common to many (mechanical) homogenization concepts is the introduction of local perturbations superimposed onto the macroscopic strain state $\boldsymbol{\varepsilon}$ in terms of

$$\boldsymbol{\varepsilon}_i = \boldsymbol{\varepsilon} + [\boldsymbol{\varepsilon}]_i, \quad (31)$$

where $i = 1, 2, 3$, in this case, represents the respective martensite variant and $[\mathbf{e}]_i$ is the related strain jump. With this in hand, the elastic part of the phase (variant) energy density reads

$$\psi_i^{\text{el}} = \frac{1}{2} [\boldsymbol{\varepsilon} + [\mathbf{e}]_i - \mathbf{e}_i^{\text{tr}}] : \mathbf{E}_i : [\boldsymbol{\varepsilon} + [\mathbf{e}]_i - \mathbf{e}_i^{\text{tr}}]. \quad (32)$$

As the main assumption of the convexification approach, these perturbations themselves are considered as minimizers of the energy density of the phase mixture

$$\psi^{\text{el}} := \sum_{i=1}^3 \xi_i \psi_i^{\text{el}}(\boldsymbol{\varepsilon}, [\mathbf{e}]_i), \quad (33)$$

so that

$$[\mathbf{e}]_i = \arg \min_{[\mathbf{e}]_i} \{\psi_i^{\text{el}}\}, \quad \text{subject to} \quad \mathbf{r}_{[\mathbf{e}]} := \sum_{i=1}^3 \xi_i [\mathbf{e}]_i = \mathbf{0}. \quad (34)$$

The constraint guarantees that the average strain is related to the phase strains through $\boldsymbol{\varepsilon} = \sum_{i=1}^3 \xi_i \mathbf{e}_i$. It is also remarked that it suffices here to only consider the elastic energy term, since all additional energy contributions do not depend on the strain jumps. By using the Lagrangian multiplier method to enforce constraint (34)₂, based on the Lagrangian

$$\mathcal{L} := \psi^{\text{el}} + \boldsymbol{\lambda} : \mathbf{r}_{[\mathbf{e}]}, \quad (35)$$

and requiring

$$\{[\mathbf{e}]_i, \boldsymbol{\lambda}\} = \arg \min_{[\mathbf{e}]_i} \max_{\boldsymbol{\lambda}} \{\mathcal{L}\}, \quad (36)$$

one obtains

$$\boldsymbol{\lambda} = \mathbf{E}_i : [\boldsymbol{\varepsilon} + [\mathbf{e}]_i - \mathbf{e}_i^{\text{tr}}] \quad \forall i = 1, 2, 3. \quad (37)$$

From this it can directly be concluded that $\boldsymbol{\lambda} = \partial_{\mathbf{e}_i} \psi_i$ represents the stress states in each phase, which are identical. It is an interesting general property of the “energy relaxation via convexification” approach that this concept coincides—in the purely mechanical case—with the Reuss-Sachs homogenization assumption known from micromechanics and thus provides a lower bound, usually associated with a more compliant material response than predicted by corresponding rank-one relaxation (laminate) based models. Furthermore, the minimization with respect to the strain jumps in (36) can be solved analytically, even for the three-variant setting. Note that the representation of these solutions is omitted here, since—as a consequence of subsequent findings—these are not necessarily required for the algorithm implementation.

As a conclusion, the phase energy densities incorporating the optimal solutions for $[\mathbf{e}]_i$ and $\boldsymbol{\lambda}$, cf. (36), can—after some straightforward algebraic manipulations—alternatively be represented as

$$\psi_i^{\text{el}} = \frac{1}{2} \boldsymbol{\lambda} : \mathbf{C}_i : \boldsymbol{\lambda}, \quad \text{with} \quad \mathbf{C}_i := \mathbf{E}_i^{-1}. \quad (38)$$

This form is particularly beneficial if the stress state in the related simulations is assumed to be homogeneously prescribed—as is the case here, where $\boldsymbol{\lambda} \equiv \bar{\boldsymbol{\sigma}}$. Based on this, the elastic contribution to the total energy density of the phase mixture is finally given by

$$\psi^{\text{el}} = \frac{1}{2} \bar{\boldsymbol{\sigma}} : \mathbf{C} : \bar{\boldsymbol{\sigma}}, \quad \text{with} \quad \mathbf{C} := \sum_{i=1}^3 \xi_i \mathbf{C}_i. \quad (39)$$

Relations (34)₂, (37) and (39)₂ can be used to show that the effective strains, which later enter the incremental potential expression, in this case take the specific form

$$\boldsymbol{\varepsilon}(\mathbf{p}^{\text{II}}) = \mathbf{C} : \bar{\boldsymbol{\sigma}} + \sum_{i=1}^3 \xi_i \mathbf{e}_i^{\text{tr}}. \quad (40)$$

The domain-specific terms related to the magnetocrystalline anisotropy energy, i.e.

$$\psi_j^{\text{ani}} = K \left[1 - \left[\frac{1}{m_s} \mathbf{m}_j^{\text{dom}} \cdot \mathbf{n}_j^{\text{ea}} \right]^2 \right], \quad \text{with} \quad j = 1, \dots, 6, \quad (41)$$

including uniaxial symmetry, are in principle identical to the corresponding energy contribution used in the laminate model. However, all possible domains illustrated in Fig. 1, and with those all easy axes represented as

$$\begin{aligned} \mathbf{n}_1^{\text{ea}} &= \mathbf{e}_1, & \mathbf{n}_2^{\text{ea}} &= -\mathbf{e}_1, & \mathbf{n}_3^{\text{ea}} &= \mathbf{e}_2, & \mathbf{n}_4^{\text{ea}} &= -\mathbf{e}_2, \\ \mathbf{n}_5^{\text{ea}} &= \mathbf{e}_3, & \mathbf{n}_6^{\text{ea}} &= -\mathbf{e}_3, \end{aligned} \quad (42)$$

are now taken into account, so that the model comprehensively includes three-dimensional effects.

In summary, the complete list of the (remaining) microstructural state variables for the convexification approach reads

$$\mathbf{p}^{\text{II}} = \{\xi_1, \xi_2, \eta_1, \eta_2, \eta_3, \mathbf{m}_1^{\text{dom}}, \dots, \mathbf{m}_6^{\text{dom}}\}. \quad (43)$$

The canonical incremental minimization principle can generally be written as

$$\mathbf{p} = \arg \min_{\mathbf{p} \in \mathcal{A}} \{ \Pi_{\text{hom}}^{\text{rel}}(\mathbf{p}) + \mathfrak{D}(\mathbf{p}, \mathbf{n}(\mathbf{p})) \}, \quad (44)$$

but \mathcal{A} in this case given by

$$\begin{aligned} r_1^{\text{II}} &:= -\xi_1 \leq 0, & r_2^{\text{II}} &:= -\xi_2 \leq 0, & r_3^{\text{II}} &:= \xi_1 - \xi_2 - 1 \leq 0, \\ r_4^{\text{II}} &:= |\eta_1| - \xi_1 \leq 0, & r_5^{\text{II}} &:= |\eta_2| - \xi_2 \leq 0, & r_6^{\text{II}} &:= |\eta_3| - [1 - \xi_1 - \xi_2] \leq 0, \\ r_{j+6}^{\text{II}} &:= \|\mathbf{m}_j^{\text{dom}}\| - m_s = 0, & j &= 1, \dots, 6. \end{aligned} \quad (45)$$

Note that, in contrast to (7), the partially-relaxed energy storage functional now incorporates the convex energy hull $C\psi(\mathbf{p})$, i.e.

$$\Pi_{\text{hom}}^{\text{rel}}(\mathbf{p}) = \left[C\psi(\mathbf{p}) + \frac{\mu_0}{2} \mathbf{m}(\mathbf{p}) \cdot \mathbf{D} \cdot \mathbf{m}(\mathbf{p}) - \mu_0 \bar{\mathbf{h}} \cdot \mathbf{m}(\mathbf{p}) - \bar{\boldsymbol{\sigma}} : \boldsymbol{\varepsilon}(\mathbf{p}) \right] V_{\mathcal{B}}. \quad (46)$$

To close the formulation of the three-variant convexification model, the contributions in (44) related to incremental energy dissipation must be specified. In extension of (27), using $\xi_3 = 1 - \xi_1 - \xi_2$, and consequentially $\dot{\xi}_3 = -\dot{\xi}_1 - \dot{\xi}_2$, the form

$$\begin{aligned} \mathfrak{D}_{\xi}^t &:= V_{\mathcal{B}} \int_0^t \left[\frac{Y_{\xi}}{\sqrt{2}} \sqrt{\dot{\xi}_1^2 + \dot{\xi}_2^2 + \dot{\xi}_3^2} \right] d\tau \\ &= V_{\mathcal{B}} \int_0^t \left[Y_{\xi} \sqrt{\dot{\xi}_1^2 + \dot{\xi}_1 \dot{\xi}_2 + \dot{\xi}_2^2} \right] d\tau, \end{aligned} \quad (47)$$

is proposed so that the related time-discretized form results in

$$\begin{aligned} \mathfrak{D} &= \mathfrak{D}_{\xi} := \mathfrak{D}_{\xi}^{t_{n+1}} - \mathfrak{D}_{\xi}^{t_n} \\ &\approx \left[Y_{\xi} \sqrt{[\xi_1 - \eta_1 \xi_1]^2 + [\xi_1 - \eta_1 \xi_1][\xi_2 - \eta_1 \xi_2] + [\xi_2 - \eta_1 \xi_2]^2} \right] V_{\mathcal{B}}. \end{aligned} \quad (48)$$

We refer to Section 4.2 concerning the detailed treatment of Y_{ξ} .

4. Algorithmic aspects

In this section, the precise treatment of the underlying equality and inequality constraints is discussed along with the overall structure of the respective algorithm related to the two model formulations.

4.1. Treatment of constraints

For the laminate model introduced in Section 3.2, the underlying model variables \mathbf{p}^{I} have been defined in (21). In view of the algorithmic treatment, the related constraints are now separated into the equality constraints

$$\tilde{\mathbf{r}}^I := \begin{bmatrix} r_5^I \\ \vdots \\ r_9^I \end{bmatrix} \stackrel{!}{=} \mathbf{0}, \quad (49)$$

and the inequality constraints

$$\hat{\mathbf{r}}^I := \begin{bmatrix} r_1^I \\ \vdots \\ r_4^I \end{bmatrix} \leq \mathbf{0}. \quad (50)$$

Similarly, for the convexification model introduced in Section 3.2, the microstructural variables \mathbf{p}^{II} have been defined in (43) and the respective arrays of equality and inequality constraints read

$$\tilde{\mathbf{r}}^{II} := \begin{bmatrix} r_7^{II} \\ \vdots \\ r_{12}^{II} \end{bmatrix} \stackrel{!}{=} \mathbf{0}, \quad (51)$$

and

$$\hat{\mathbf{r}}^{II} := \begin{bmatrix} r_1^{II} \\ \vdots \\ r_6^{II} \end{bmatrix} \leq \mathbf{0}. \quad (52)$$

For the algorithmic implementation of these, an Augmented Lagrangian approach is used in general. This became necessary due to the fact that the use of “black box” schemes from common libraries did not yield satisfactory results. More specifically, penalty functions according to Bertsekas (1982) are utilized, viz.

$$\tilde{\mathfrak{P}}^\bullet := \sum_{p=1}^{n_{\text{con}}^\bullet} \left[\lambda_p \tilde{r}_p^\bullet + \frac{1}{2} \tilde{\chi} |\tilde{r}_p^\bullet|^2 \right], \quad (53)$$

with respect to the equality constraints, and

$$\hat{\mathfrak{P}}^\bullet := \frac{1}{2\hat{\chi}} \left[\sum_{p=1}^{\hat{n}_{\text{con}}} \left[\left[\max \{0, \mu_p + \hat{\chi} \hat{r}_p^\bullet\} \right]^2 - \mu_p^2 \right] \right] \quad (54)$$

with respect to the inequality constraints. The symbol \bullet is a placeholder for the respective modeling approach, thus $\bullet \in \{I, II\}$. The quantities $\tilde{n}_{\text{con}}^\bullet$ denote the total number of equality constraints for the respective modeling approach, whereas $\hat{n}_{\text{con}}^\bullet$ stands for the total number of respectively underlying inequality constraints. More precisely speaking, one has $\tilde{n}_{\text{con}}^I = 5$, $\hat{n}_{\text{con}}^I = 4$, $\tilde{n}_{\text{con}}^{II} = 6$, and $\hat{n}_{\text{con}}^{II} = 6$. With these quantities at hand, the formerly constrained minimization problem is transferred into an unconstrained minimization problem of the form

$$\mathbf{p}^\bullet = \arg \min \left\{ \Pi_{\text{hom}}(\mathbf{p}^\bullet) + \mathfrak{D}(\mathbf{p}^\bullet, {}^n\mathbf{p}^\bullet) + \tilde{\mathfrak{P}}^\bullet(\mathbf{p}^\bullet) + \hat{\mathfrak{P}}^\bullet(\mathbf{p}^\bullet) \right\}. \quad (55)$$

As standard for the pursued method, the Lagrange-type multipliers $\tilde{\chi}$, λ_p , $\hat{\chi}$, and μ_p have to be initially chosen and iteratively adjusted in order to fulfill the constraints up to a chosen tolerance. The precise procedure to solve (55) and how the underlying penalty coefficients are updated will be elaborated in the subsequent section.

4.2. Specific algorithms

It turned out, that a straight-forward implementation of the underlying minimization problem given by (55) did not result in stable schemes and furthermore no satisfactory results for both models presented here. As a consequence, the minimization that

underlies both modeling approaches is carried out in a staggered scheme instead of a monolithic procedure. The following subsections are therefore devoted to the precise discussion of the specifically developed algorithm. Note, that the structure of both algorithms are very similar and that the main ideas are essentially identical.

4.2.1. Algorithm 1: laminate model

The structure of algorithm 1 for the implementation of the laminate model is depicted in Table 2. In the following, some of the most essential steps of the algorithm shall be discussed in detail:

- step 1d is only required to initially pass step 2.
- step 1e is necessary or at least helpful to trigger the initiation of martensite reorientation in the correct time step. The precise values used here are $\xi^{\text{down}} = 0.2$, $\xi^{\text{up}} = 0.8$. These values should sufficiently differ from zero and one, respectively, in order to push the algorithm towards the global minimum of the underlying energy potential. Without this approach, the algorithm tends to predict the onset of variant switching too late. This is justified by related local minimum paths, the algorithm would follow for too long without this modification. These more or less arbitrarily chosen values result in sufficiently stable calculations. There is, however, no evidence that these chosen values are optimal.
- step 2: The minimization procedure is not finished until two (almost) identical results are obtained. The indicator for “identical results” is the difference between two energy values obtained in subsequent loops.
- steps 2, 5c, 6d, ..., 10d: The tolerances are chosen as $TOL_\Pi = 10^{-6}$, $TOL_n = 10^{-5}$, $TOL_m = 10^{-2}$, and $TOL_{\xi\eta} = 10^{-7}$.
- step 3a: It turned out to be inevitable to initialize the penalty-related parameters at this point in order to obtain satisfactory results and to ensure numerical stability. The initial values are chosen as $\tilde{\chi}^{\text{init}} = 10^{-5}$, $\hat{\chi}^{\text{init}} = 10^8$. These values were determined by trial and error and they led to sufficiently stable calculations. Again, there is no evidence that these values are optimal.
- steps 5d, 6e, ..., 10e: The scaling factors are chosen as $scal_{\tilde{\chi}} = 10$, $scal_{\hat{\chi}} = 10$.
- step 6a, ...: To increase the algorithm's efficiency, the minimization w.r.t the local magnetization $\mathbf{m}_j^{\text{dom}}$ is only carried out if the respective domain volume fraction α_j is significantly different from zero, where a threshold of 10^{-3} is used.
- steps 10d, e: $\langle x \rangle := \max\{0, x\}$
- step 12: a reset of κ is necessary, if the material should consist of a single phase, i.e. $\xi_1 = 1$ or $\xi_1 = 0$. If this holds, ${}^{n+1}\kappa = 0$.

It is remarked that this procedure is executed with ${}^0\kappa = 0$ for the initial time step 0t and, moreover, that in this case all dissipative effects are neglected, i.e. $\mathfrak{D} \equiv 0$.

4.2.2. Algorithm 2: convexification model

The structure of algorithm 2 for the implementation of the convexification model is depicted in Table 3. The main and important aspects of the algorithm are similar to the ones mentioned in Section 4.2.1, where these may refer to different steps in the algorithmic sequence here. Also, the values for the underlying tolerances, scaling factors, and the like are chosen identically (whereby TOL_n is not required here). In addition, the approach for $t = {}^0t$ is analogous to what is described above.

Table 2

Algorithm 1 (laminate model).

1. **Initialization** (time step $n+1$ with $n \geq 0$):
 - 1a. set $k = 0$
 - 1b. set ${}^k \mathbf{p}^I = {}^n \mathbf{p}$
 - 1c. calculate ${}^k \Pi^I := \Pi^I({}^n \mathbf{p}^I, {}^{n+1} \bar{\boldsymbol{\sigma}}, {}^{n+1} \bar{\mathbf{h}})$ where $\Pi^I \triangleq \Pi_{\text{hom}}$ according to (24)
 - 1d. set $\Pi^{\text{ref}} \gg {}^k \Pi^I$
 - 1e. if ${}^k \xi_1 < \xi^{\text{down}}$ then set ${}^k \xi_1 = \xi^{\text{down}}$, if ${}^k \xi_1 > \xi^{\text{up}}$ then set ${}^k \xi_1 = \xi^{\text{up}}$
2. **Check convergence**
 - if $|[{}^k \Pi^I - \Pi^{\text{ref}}] / \Pi^{\text{ref}}| \leq \text{tol}_{\Pi}$ then go to step 12
3. **Initialize penalty parameter**
 - 3a. set $\lambda_p = 0, \mu_p = 0, \tilde{\chi} = \tilde{\chi}^{\text{init}}, \hat{\chi} = \hat{\chi}^{\text{init}}$
 - 3b. set $\Pi^{\text{ref}} = {}^k \Pi^I$
4. **Determine \mathbf{a}**
 - 4a. define ${}^{k+1} \Pi_{\mathbf{a}}^I := \Pi^I({}^k \xi_1, {}^k \eta_1, {}^k \eta_2, {}^{k+1} \mathbf{a}, {}^k \mathbf{n}, {}^k \mathbf{m}_1^{\text{dom}}, \dots, {}^k \mathbf{m}_4^{\text{dom}})$
 - 4b. determine ${}^{k+1} \mathbf{a} = \arg \min \{{}^{k+1} \Pi_{\mathbf{a}}^I\}$
5. **Determine \mathbf{n}**
 - 5a. define ${}^{k+1} \Pi_{\mathbf{n}}^I := \Pi^I({}^k \xi_1, {}^k \eta_1, {}^k \eta_2, {}^{k+1} \mathbf{a}, {}^{k+1} \mathbf{n}, {}^k \mathbf{m}_1^{\text{dom}}, \dots, {}^k \mathbf{m}_4^{\text{dom}})$
 - 5b. determine ${}^{k+1} \mathbf{n} = \arg \min \{{}^{k+1} \Pi_{\mathbf{n}}^I + \lambda_1 \tilde{r}_1^I + 1/2 \tilde{\chi} |\tilde{r}_1^I|^2\}$
 - 5c. if $\tilde{r}_1^I \leq \text{tol}_{\mathbf{n}}$ then go to step 6a.
 - 5d. update $\lambda_1 \leftarrow \lambda_1 + \tilde{\chi} \tilde{r}_1^I, \tilde{\chi} \leftarrow \text{scal}_{\tilde{\chi}} \tilde{\chi}$, go to step 5b
6. **Determine $\mathbf{m}_1^{\text{dom}}$**
 - 6a. if $k\alpha_1 \approx 0$ then go to step 7
 - 6b. define ${}^{k+1} \Pi_{\mathbf{m}_1}^I := \Pi^I({}^k \xi_1, {}^k \eta_1, {}^k \eta_2, {}^{k+1} \mathbf{a}, {}^{k+1} \mathbf{n}, {}^{k+1} \mathbf{m}_1^{\text{dom}}, \dots, {}^k \mathbf{m}_4^{\text{dom}})$
 - 6c. determine ${}^{k+1} \mathbf{m}_1^{\text{dom}} = \arg \min \{{}^{k+1} \Pi_{\mathbf{m}_1}^I + \lambda_2 \tilde{r}_2^I + 1/2 \tilde{\chi} |\tilde{r}_2^I|^2\}$
 - 6d. if $\tilde{r}_2^I \leq \text{tol}_{\mathbf{m}}$ then go to step 7
 - 6e. update $\lambda_2 \leftarrow \lambda_2 + \tilde{\chi} \tilde{r}_2^I, \tilde{\chi} \leftarrow \text{scal}_{\tilde{\chi}} \tilde{\chi}$, go to step 6c
7. **Determine $\mathbf{m}_2^{\text{dom}}$**
 - analogous to steps 6a to 6e, determine ${}^{k+1} \mathbf{m}_2^{\text{dom}}$ by using λ_3 and \tilde{r}_3^I
8. **Determine $\mathbf{m}_3^{\text{dom}}$**
 - analogous to steps 6a to 6e, determine ${}^{k+1} \mathbf{m}_3^{\text{dom}}$ by using λ_4 and \tilde{r}_4^I
9. **Determine $\mathbf{m}_4^{\text{dom}}$**
 - analogous to steps 6a to 6e, determine ${}^{k+1} \mathbf{m}_4^{\text{dom}}$ by using λ_5 and \tilde{r}_5^I
10. **Determine ξ_1, η_1, η_2**
 - 10a. define ${}^{k+1} \Pi_{\xi\eta}^I := \Pi^I({}^{k+1} \xi_1, {}^{k+1} \eta_1, {}^{k+1} \eta_2, {}^{k+1} \mathbf{a}, {}^{k+1} \mathbf{n}, {}^{k+1} \mathbf{m}_1^{\text{dom}}, \dots, {}^{k+1} \mathbf{m}_4^{\text{dom}})$
 - 10b. set ${}^{n+1} \kappa = n\kappa + |{}^{k+1} \xi_1 - n\xi_1|$
 - 10c. determine $\{{}^{k+1} \xi_1, {}^{k+1} \eta_1, {}^{k+1} \eta_2\} = \arg \min \{{}^{k+1} \Pi_{\xi\eta}^I + \mathfrak{D}({}^{k+1} \mathbf{p}, {}^n \mathbf{p}) + \hat{\Phi}^I\}$
 - 10d. if $\|\langle \tilde{r}_1^I \rangle, \dots, \langle \tilde{r}_4^I \rangle\| \leq \text{tol}_{\xi\eta}$ then go to step 11
 - 10e. update $\mu_p \leftarrow \langle \mu_p + \hat{\chi} \tilde{r}_p^I \rangle, p = 1, \dots, 4, \tilde{\chi} \leftarrow \text{scal}_{\tilde{\chi}} \tilde{\chi}$, go to step 10c
11. **Redefine current energy value**
 - calculate ${}^{k+1} \Pi^I = \Pi^I({}^{k+1} \mathbf{p}^I)$, update $k \leftarrow k + 1$, go to step 2
12. **Completion of iteration**
 - set ${}^{n+1} \mathbf{p}^I = {}^{k+1} \mathbf{p}^I$, reset κ if necessary, update $n \leftarrow n + 1$, go to step 1a

5. Numerical examples

In this section, the predictive capabilities of both modeling frameworks are investigated and compared. First, a verification example is presented as a proof of concept, to test whether both extended models—and their algorithmic treatments and implementations—recover special case solutions predicted by the two-dimensional formulation summarized in Table 1, see also Bartel et al. (2020). In a second numerical example, the experimental setup presented in Feigenbaum et al. (2016) is taken as motivation for a fully three-dimensional loading scenario, for which response simulations would not be possible with the original model. To this end, we discuss predictions obtained from the three-variant convexification model, with three-dimensionally parameterized microstructural variable vectors, as proposed in Section 3.2.

Note that for the specific examples discussed here, identical isotropic elasticity tensors, as specified in (16), are assumed for each phase, even though the formulations generally allow arbitrary anisotropy—see, for example, (19) and (32). This is a small caveat owed to the fact that the elastic constants of the 5 M modulated

Table 3

Algorithm 2 (convexification model).

1. **Initialization** (time step $n+1$ with $n \geq 0$):
 - 1a. set $k = 0$
 - 1b. set ${}^k \mathbf{p}^{\text{II}} = {}^n \mathbf{p}$
 - 1c. calculate ${}^k \Pi^{\text{II}} := \Pi^{\text{II}}({}^n \mathbf{p}^{\text{II}}, {}^{n+1} \bar{\boldsymbol{\sigma}}, {}^{n+1} \bar{\mathbf{h}})$ where $\Pi^{\text{II}} \triangleq \Pi_{\text{hom}}^{\text{rel}}$ according to (46)
 - 1d. set $\Pi^{\text{ref}} \gg {}^k \Pi^{\text{II}}$
 - 1e. if ${}^k \xi_1 < \xi^{\text{down}}$ then set ${}^k \xi_1 = \xi^{\text{down}}$, if ${}^k \xi_1 > \xi^{\text{up}}$ then set ${}^k \xi_1 = \xi^{\text{up}}$
 - if ${}^k \xi_2 < \xi^{\text{down}}$ then set ${}^k \xi_2 = \xi^{\text{down}}$, if ${}^k \xi_2 > \xi^{\text{up}}$ then set ${}^k \xi_2 = \xi^{\text{up}}$
2. **Check convergence**
 - if $|[{}^k \Pi^{\text{II}} - \Pi^{\text{ref}}] / \Pi^{\text{ref}}| \leq \text{tol}_{\Pi}$ then go to step 12
3. **Initialize penalty parameter**
 - 3a. set $\lambda_p = 0, \mu_p = 0, \tilde{\chi} = \tilde{\chi}^{\text{init}}, \hat{\chi} = \hat{\chi}^{\text{init}}$
 - 3b. set $\Pi^{\text{ref}} = {}^k \Pi^{\text{II}}$
4. **Determine $\mathbf{m}_1^{\text{dom}}$**
 - 4a. if $k\alpha_1 \approx 0$ then go to step 5
 - 4b. define ${}^{k+1} \Pi_{\mathbf{m}_1}^{\text{II}} := \Pi^{\text{II}}({}^k \xi_1, {}^k \xi_2, {}^k \eta_1, {}^k \eta_2, {}^k \eta_3, {}^{k+1} \mathbf{m}_1^{\text{dom}}, \dots, {}^k \mathbf{m}_6^{\text{dom}})$
 - 4c. determine ${}^{k+1} \mathbf{m}_1^{\text{dom}} = \arg \min \{{}^{k+1} \Pi_{\mathbf{m}_1}^{\text{II}} + \lambda_1 \tilde{r}_1^{\text{II}} + 1/2 \tilde{\chi} |\tilde{r}_1^{\text{II}}|^2\}$
 - 4d. if $\tilde{r}_1^{\text{II}} \leq \text{tol}_{\mathbf{m}}$ then go to step 5
 - 4e. update $\lambda_1 \leftarrow \lambda_1 + \tilde{\chi} \tilde{r}_1^{\text{II}}, \tilde{\chi} \leftarrow \text{scal}_{\tilde{\chi}} \tilde{\chi}$, go to step 4c
5. **Determine $\mathbf{m}_2^{\text{dom}}$**
 - analogous to steps 4a to 4e, determine ${}^{k+1} \mathbf{m}_2^{\text{dom}}$ by using λ_2 and \tilde{r}_2^{II}
6. **Determine $\mathbf{m}_3^{\text{dom}}$**
 - analogous to steps 4a to 4e, determine ${}^{k+1} \mathbf{m}_3^{\text{dom}}$ by using λ_3 and \tilde{r}_3^{II}
7. **Determine $\mathbf{m}_4^{\text{dom}}$**
 - analogous to steps 4a to 4e, determine ${}^{k+1} \mathbf{m}_4^{\text{dom}}$ by using λ_4 and \tilde{r}_4^{II}
8. **Determine $\mathbf{m}_5^{\text{dom}}$**
 - analogous to steps 4a to 4e, determine ${}^{k+1} \mathbf{m}_5^{\text{dom}}$ by using λ_5 and \tilde{r}_5^{II}
9. **Determine $\mathbf{m}_6^{\text{dom}}$**
 - analogous to steps 4a to 4e, determine ${}^{k+1} \mathbf{m}_6^{\text{dom}}$ by using λ_6 and \tilde{r}_6^{II}
10. **Determine $\xi_1, \eta_1, \eta_2, \eta_3$**
 - 10a. define ${}^{k+1} \Pi_{\xi\eta}^{\text{II}} := \Pi^{\text{II}}({}^{k+1} \xi_1, {}^{k+1} \xi_2, {}^{k+1} \eta_1, {}^{k+1} \eta_2, {}^{k+1} \eta_3, {}^{k+1} \mathbf{m}_1^{\text{dom}}, \dots, {}^{k+1} \mathbf{m}_6^{\text{dom}})$
 - 10b. set ${}^{n+1} \kappa = n\kappa + \sqrt{[{}^{n+1} \xi_1 - n\xi_1]^2 + [{}^{n+1} \xi_2 - n\xi_2]^2 + [{}^{n+1} \eta_2 - n\eta_2]^2}$
- 10c. determine $\{{}^{k+1} \xi_1, {}^{k+1} \xi_2, {}^{k+1} \eta_1, {}^{k+1} \eta_2, {}^{k+1} \eta_3\} = \arg \min \{{}^{k+1} \Pi_{\xi\eta}^{\text{II}} + \mathfrak{D}({}^{k+1} \mathbf{p}, {}^n \mathbf{p}) + \hat{\Phi}^{\text{II}}\}$
- 10d. if $\|\langle \tilde{r}_1^{\text{II}} \rangle, \dots, \langle \tilde{r}_6^{\text{II}} \rangle\| \leq \text{tol}_{\xi\eta}$ then go to step 11
- 10e. update $\mu_p \leftarrow \langle \mu_p + \hat{\chi} \tilde{r}_p^{\text{II}} \rangle, p = 1, \dots, 6, \tilde{\chi} \leftarrow \text{scal}_{\tilde{\chi}} \tilde{\chi}$, go to step 10c

- 11. **Redefine current energy value**
- calculate ${}^{k+1} \Pi^{\text{II}} = \Pi^{\text{II}}({}^{k+1} \mathbf{p}^{\text{II}})$, update $k \leftarrow k + 1$, go to step 2
- 12. **Completion of iteration**
- set ${}^{n+1} \mathbf{p}^{\text{II}} = {}^{k+1} \mathbf{p}^{\text{II}}$, reset κ if necessary, update $n \leftarrow n + 1$, go to step 1a

martensite in Ni-Mn-Ga—to which we typically compare our simulations, cf. Bartel et al. (2020)—have not been reported in the literature with sufficient accuracy. In contrast to the non-modulated Ni-Mn-Ga martensite, there exist technical difficulties in characterizing the anisotropic elastic properties of the modulated variety, since it is practically impossible in this case to prepare a twin-free single-variant sample required for such measurements. We refer to the discussion in Dai et al. (2004), Sedláček et al. (2017), Ozdemir and Cagin (2010) for more details.

Furthermore, the coefficients of the demagnetization tensor (shape factors) introduced in (18), have specifically been calculated as

$$\mathbf{D} = 0.2154 \mathbf{e}_1 \otimes \mathbf{e}_1 + 0.3923 [\mathbf{e}_2 \otimes \mathbf{e}_2 + \mathbf{e}_3 \otimes \mathbf{e}_3], \quad \text{with } \text{tr} \mathbf{D} = 1, \quad (56)$$

via three-dimensional magnetostatic finite element analysis, for a prismatic sample aligned with the coordinate axes and of size $9 \text{ mm} \times 5 \text{ mm} \times 5 \text{ mm}$ —the dimensions used in the reference experiments (Heczko, 2005).

The material constants used for all simulations are listed in Table 4.

It should be mentioned here, that classical magnetostriction is not considered in the constitutive framework at hand. This is mainly due to the fact that the related strains can be considered negligible, particularly in comparison to the transformation strains arising from variant switching.

Table 4

Material parameters for Ni₂MnGa (slightly off-stoichiometric composition with five-layered modulated tetragonal structure), cf. Heczko et al. (2003), Straka et al. (2003) and Heczko (2005).

Model parameter	Symbol	Value	Unit
Young's modulus	E	5000.0	MPa
Poisson's ratio	ν	0.3	—
Saturation magnetization	m_s	514.0	kA/m
Anisotropy constant	K	0.1365	MJ/m ³
Dissipation parameter	γ_ξ	0.03	MJ/m ³
Dissipation parameter	$\Delta\gamma_\xi$	0.029	MJ/m ³
Bain strain coefficient	b_1	0.0188	—
Bain strain coefficient	b_2	−0.0394	—

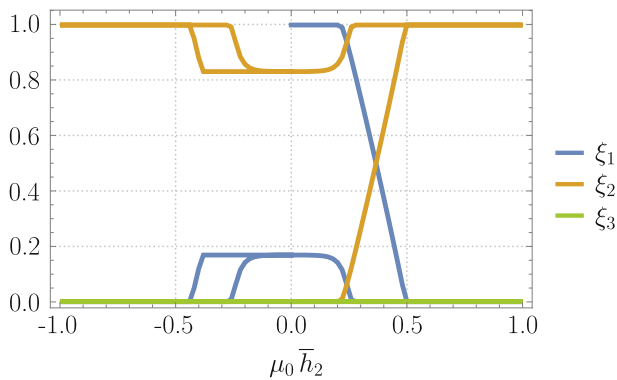
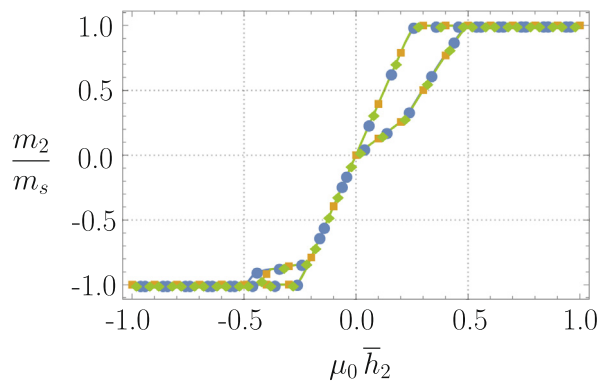
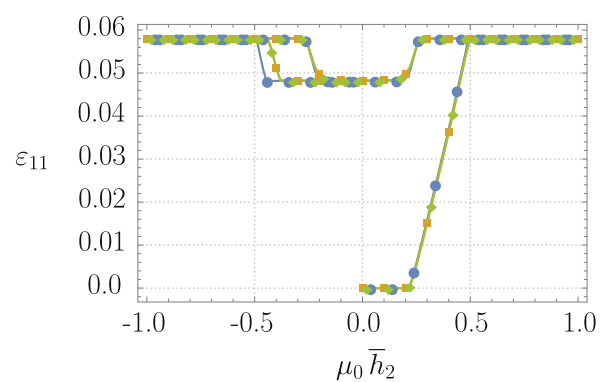


Fig. 2. Evolution of the martensite variant volume fractions under a cyclically prescribed transverse magnetic field $\bar{h}_2(t)$ at a constant axial compressive stress of $\bar{\sigma}_{11} = -0.6$ MPa obtained by the convexification approach (model II). As can be concluded from Fig. 3, these would fully match the predictions obtained by the laminate approach (model I) and also—with slight deviations—the original model (cf. Table 1).



(a) Magnetic field-induced magnetization hysteresis.



(b) Magnetic field-induced strain (butterfly) hysteresis.

● original ■ model I ◆ model II

Fig. 3. Predicted effective sample responses in terms of (a) magnetization and (b) straining behavior under a cyclically prescribed transverse magnetic field $\bar{h}_2(t)$ at a constant axial compressive stress of $\bar{\sigma}_{11} = -0.6$ MPa. The results are virtually identical for the laminate approach (model I) and the convexification approach (model II). They also match the predictions of the original model (cf. Table 1) to a large extent. Slight deviations occur when variant 1, which partially re-evolves during unloading, starts to transform back into variant 2. The reason for this lies in the fact that the algorithm used for the original model taken from Bartel et al. (2020) predicts the onset of reverse switching too late. A quantitative proof is provided in the text. Note, that only selected data points are shown by the respective markers.

5.1. Proof of concept

In this first verification example, the mechanical and magnetic loading of the prismatic Ni₂MnGa sample is applied in two different stages:

1. Starting from an unloaded state, a uniaxially applied compressive stress is linearly increased up to $\bar{\sigma}_{11} = -0.6$ MPa, in the absence of an external magnetic field. The loading was applied in 20 equidistant steps.
2. While keeping the stress state constant at the maximum load level of step 1, the magnetic field is linearly increased up to $\mu_0 \bar{h}_2 = 1.0$ T, then linearly decreased to $\mu_0 \bar{h}_2 = -1.0$ T, and finally again increased to reach $\mu_0 \bar{h}_2 = 0.0$ T. The loading was applied in 200 equidistant steps.

This loading scenario corresponds to the most common experimental setup for MSMA single crystal testing, cf. Tickle et al., 1999; Heczko et al., 2000; Heczko et al., 2003; Straka et al., 2003; Heczko, 2005; Kiefer et al., 2007; Straka, 2007.

The predicted response curves are shown in Figs. 2 and 3, respectively. In these results, simulations based on the extended laminate model I (cf. algorithm 1 summarized in Table 2) and fully three-dimensional convexification model II (cf. algorithm 2 summarized in Table 3) are compared to the original two-dimensional, two-variant laminate approach, for which detailed numerical tests were recently presented in Bartel et al. (2020). Note that only the simulation results corresponding to the second loading stage are illustrated in these figures. The first loading stage merely serves the purpose of producing a well-defined initial (single-variant 1) state as is, in fact, also common practice in the experiments. The offset strains occurring during loading stage 1 have been reset for the subsequent figures for illustration purposes. These offset strains are, however, fully considered in the calculations.

As shown in Fig. 2, the second (magnetic field-favored) martensite variant is predicted to grow at the expense of the first (compressive stress-favored) variant during magnetic field loading at constant stress. For maximum loading—in the positive and negative half-cycles—the material fully consists of martensite variant 2, at this particular stress level. It is also observed, however, that the bias

stress is too low to return the microstructure to the stress-favored single-variant 1 state during magnetic unloading. In this example, only about 20% of variant 1 is recovered and then again fully transformed into variant 2 with magnetic field loading in the opposite direction. This phenomenon, which is nicely captured by all models under consideration, has been termed the *first cycle effect*, see Kiefer and Lagoudas (2005), as the second and following cycles would show a stably-symmetric field-induced variant switching—and therefore strain, see Fig. 3(b)—butterfly-type hysteresis behavior. It was previously demonstrated in Bartel et al. (2020) that these predictions also match experimental data very well.

Most important in the context of the current contribution, however, is the fact that the extended laminate approach (model I) as

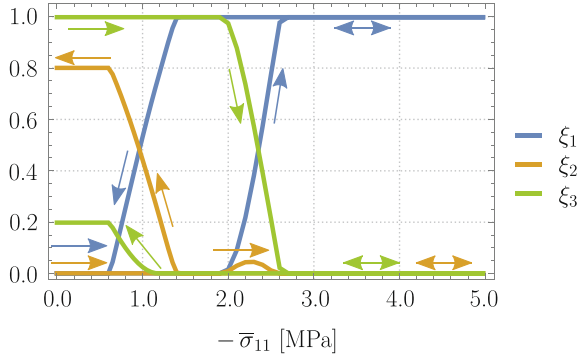


Fig. 4. Predictions by the extended convexification formulation: Evolution of the martensite variant volume fractions due to a cyclically prescribed axial compressive stress $\bar{\sigma}_{11}(t)$ at a constant transverse stress of $\sigma_{33} = -1.5$ MPa and a constant magnetic field of $\mu_0 \bar{h}_2 = 0.45$ T. Arrows indicate the progression of the curves.

well as the fully three-dimensional convexification approach clearly recover the result of the original model—as expected for this special case. In particular, although generally possible in model II, the third variant is never activated in the simulations of this loading scenario. Moreover, the much more complex three-dimensional parameterization of the vector-valued microstructural variables (domain magnetizations in model II and, additionally, the vectors describing the strain jump and twin-interface orientation in model I), does not introduce any unexpected deviations from the reference solution. Particular attention should be paid to the slight differences in the results. While both of the newly presented approaches yield equal results, those of the original model slightly differ in one specific region of the loading path. As can be observed from Fig. 3(b), both models I and II predict an earlier onset of reverse switching compared to the original model. This gives rise to the question which of the algorithms can be considered (more) reliable. The answer is, that indeed the new algorithms yield more accurate results, which is verified by the following consideration: Specific values of the minimized energy potential $\mathcal{L}^k := \Pi_{\text{hom}}(k, \mathbf{p}) + \mathcal{D}(k, \mathbf{p} - k^{-1} \mathbf{p})$ at time/load step k shall be compared, namely (i) the value obtained by the original model resulting in $\mathcal{L}_{\text{org}}^k$, and (ii) the value obtained by model I which yields \mathcal{L}_1^k . After undergoing the first loading–unloading cycle and reaching $\mu_0 \bar{h}_2 = -0.44$ T, which corresponds to $k = 123$, the original model still predicts no initiation of reverse switching, while model I already predicts its completion. At this point, the relative deviation is $[\mathcal{L}_1^{123} - \mathcal{L}_{\text{org}}^{123}] / \mathcal{L}_{\text{org}}^{123} = -4.1\%$. As a conclusion, the prediction of an earlier onset and completion of the reverse switching process results in significantly lower energy states. Therefore it can be stated, that the new algorithm yields more accurate results and, vice

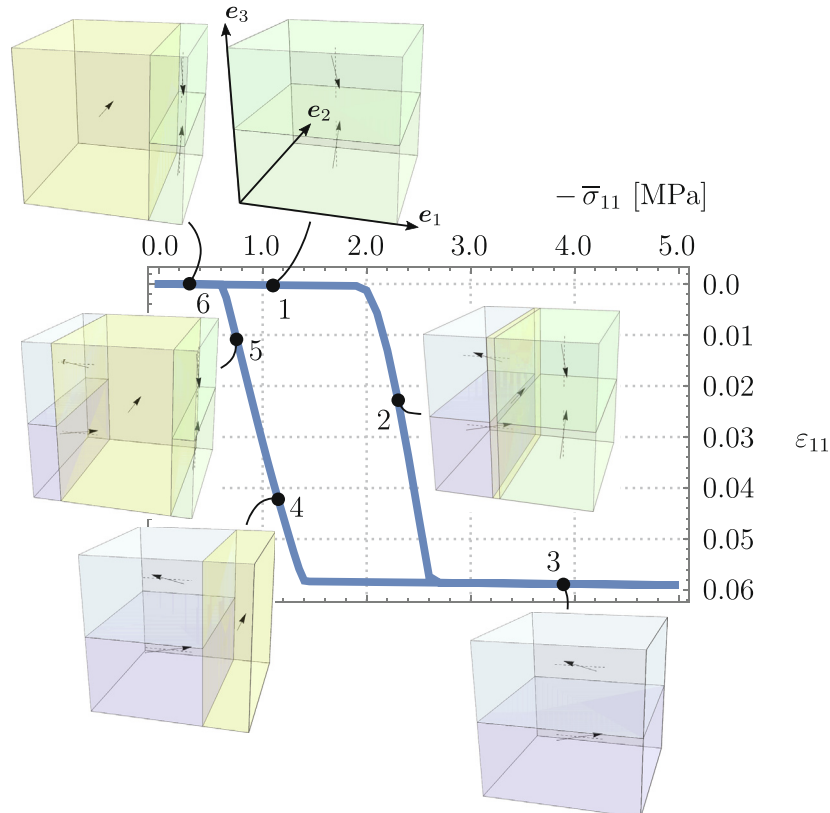


Fig. 5. Simulated stress–strain behavior of the sample in response to a cyclically prescribed axial compressive stress $\bar{\sigma}_{11}(t)$ at a constant transverse stress of $\sigma_{33} = -1.5$ MPa and a constant magnetic field of $\mu_0 \bar{h}_2 = 0.45$ T. The microstructural sketches quantitatively indicate current domain volume fractions and magnetization vector orientations.

versa, that the algorithm used in Bartel et al. (2020) for the original model exhibits some shortcomings, particularly in this region of the loading path.

We therefore consider the extended model formulations—and their novel algorithmic treatments—as sufficiently verified with respect to this two-dimensional loading case.

5.2. A fully three-dimensional loading case

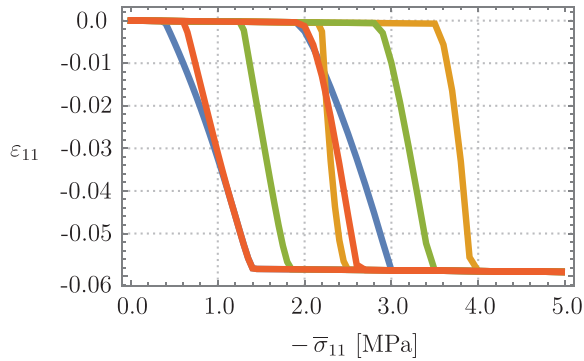
Inspired by the experimental setup described in Feigenbaum et al. (2016), the loading is applied in three stages in this second class of simulations:

1. Starting from an unloaded state, a transverse compressive stress is applied and linearly increased up to $\bar{\sigma}_{33} = -1.5$ MPa, referred to as “lateral load” in Feigenbaum et al. (2016). The loading was applied in 50 equidistant steps.
2. While keeping the transverse bias stress state constant at the maximum load level of step 1, a transverse magnetic field is applied and linearly increased up to $\mu_0 \bar{h}_2 = 0.45$ T. The loading was applied in 50 equidistant steps.
3. Still keeping the transverse stress $\bar{\sigma}_{33}$ and now also the transverse magnetic field \bar{h}_2 constant at maximum levels, a time varying axial stress is applied, linearly increased up to

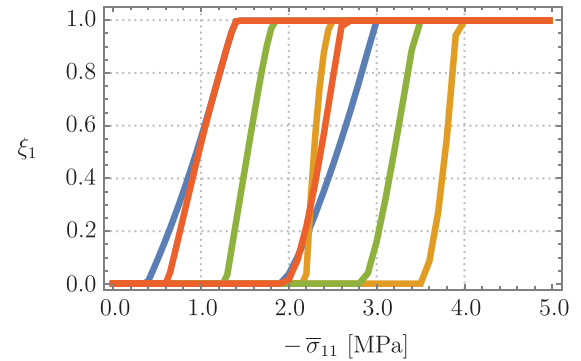
$\bar{\sigma}_{11}(t) = 5.0$ MPa and subsequently decreased (back) to zero. The loading was applied in 200 equidistant steps.

Due to the fact that the extended convexification approach is the only framework discussed here which takes all martensite variants into account, the numerical examples in this section are restricted to model II (cf. algorithm 2 summarized in Table 3). The corresponding response predictions are shown in Figs. 4–6. All results illustrated in this section refer to the third loading stage. The first stage serves the purpose of setting up a well-defined initial configuration, while the second introduces a magneto-mechanical bias state that helps to induce all three variants during the uniaxial stress cycling in stage 3. The offset strains occurring during loading stages 1 and 2 have been reset for the subsequent figures for illustration purposes and for the sake of more intuitive comparisons. These offset strains are, however, fully considered in the calculations.

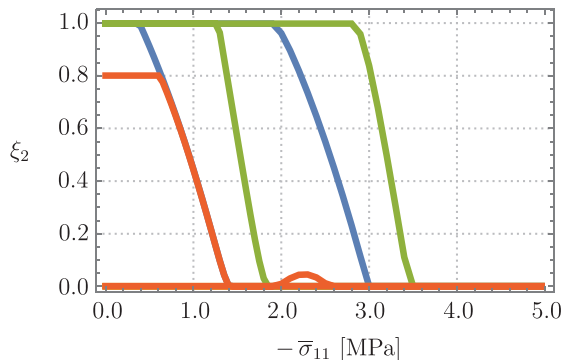
Fig. 4, which shows the evolution of the variant volume fractions, confirms that indeed an initial single-variant state was achieved by means of the first loading stage—in this case it is entirely comprised of variant 3. It can further be concluded that the magnetic field bias of the second loading stage, which favors variant 2, is not strong enough to overcome the favoring of variant 3 by the transverse stress. In the context of such observations, the reader is referred to Fig. 1, which shows very instructive and lends



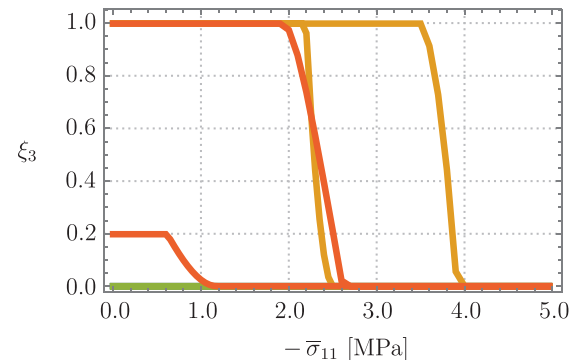
(a) Axial straining under stress-induced variant switching.



(b) Evolution of variant volume fraction ξ_1 .



(c) Evolution of variant volume fraction ξ_2 .



(d) Evolution of variant volume fraction ξ_3 .



Fig. 6. Predicted effective sample responses in terms of (a) axial straining and (b)–(d) variant volume fractions under a cyclically prescribed axial compressive stress $\bar{\sigma}_{11}(t)$ for different constant bias values of $\bar{\sigma}_{33}$ and \bar{h}_2 .

intuition as to what should happen with respect to variant switching under different magneto-mechanical loadings. For instance, compressive stresses promote variants whose respective unit cell short axis is aligned with the loading direction, whereas tensile stresses do the opposite. Moreover, magnetic fields favor the variant (and domain) type whose easy axis is oriented in the respective direction of loading.

It is then observed at around $\bar{\sigma}_{11} = -2.0$ MPa that variant 3 to variant 1 switching is mechanically induced, which is later completed at an axial compressive stress of about -2.7 MPa. Interestingly, at an intermediate load level, a small amount of variant 2 momentarily also appears, so that all three variants coexist there. Apparently, neither the transverse stress biasing of variant 3, nor the variant 2 bias through the transverse magnetic field, nor the favoring of variant 1 by the increasing axial stress are able to completely dominate the other driving forces for switching at this particular combination of loads. After loading reversal, the single variant 1 state is stable until $\bar{\sigma}_{11} \approx -1.4$ MPa, at which point variant 2 is re-induced, followed by a re-induced variant 3 shortly thereafter but with a lower growth rate than variant 2. Finally, the material consists of roughly a 80/20 volume percent mixture of those two variants at zero axial stress, which marks the end of the second numerical test. From this first set of results it can be concluded that the extended convexification formulation (model II) is indeed capable of handling loading cases, in which all three tetragonal martensite variants may physically appear and the switching between them—and any of their combinations—should generally be possible.

This conclusion is further supported by the corresponding stress–strain curves shown in Fig. 5, where domain volume fractions and local magnetization vector orientations have also been visualized for six selected load levels. These sketches highlight another aspect of the MSMA model extension, namely the fully-three dimensional parameterization of the magnetization vectors. These were already present during the first, entirely two-dimensional, numerical example, but not fully activated there. These sketches in Fig. 5 do not reflect actual microstructural arrangements—information such as twin boundary and domain interface orientations or twin band widths are not included and therefore not available within the convexification approach. However, these illustrations are quantitatively accurate visualizations of the microstructural variables, see (43), and therefore immensely helpful in understanding the correlation between microstructure and effective responses as predicted by the extended convexification model under complex multi-dimensional magneto-mechanical loading.

The sketch marked as state 1 in Fig. 5 shows that for this particular numerical test both domain types of variant 3 initially coexist in equal shares, with magnetization vectors slightly rotated towards the \bar{h}_2 bias field. The first significant change in the strain evolution occurs at the initiation of variant reorientation, where the two domains types of variant 1 form with identical volume fractions, as seen in state 2. Similar to the domains in variant 1, their local magnetizations are also rotated away from the respective easy axis, to accommodate the \bar{h}_2 field. Furthermore, in state 2 the discussed and rather small amount of a single-domain variant 2 martensite appears, whose magnetization remains perfectly aligned with its easy axis, since this axis is already oriented in the direction of the prescribed magnetic field. State 3 shows the values of the microstructural state variables after completion of all switching processes during loading. At this point, not only variant 1 is eliminated, but variant 2 has also vanished, so that only variant 1 remains with equally sized domains. The conditions during unloading favor the formation of variant 2 (see state 4), with a single domain type. However, a three-variant configuration is also

encountered here (see state 5) at a load level, where the applied axial stress is too low to prevent the transverse stress bias from nucleating variant 3. Finally, as depicted for state 6—and consistent with what was observed in Fig. 4—a variant 2/3 mixture remains at the end of the loading cycle. Throughout the entire loading sequence, the rotation of the magnetization vectors away from their respective easy axes remains the same, since the bias field is kept constant. For the same reason, the domain volume fractions within each variant remains equal (yielding $\eta_j = 0$, for $j = 1, 2, 3$), although their combined volume fractions, i.e. the variant volume fraction ξ_j , change.

To further investigate the predictive capabilities of the extended convexification model, we consider a number of variations of the second loading scenario, by altering the stress and magnetic field bias values prescribed during loading stages 1 and 2. Fig. 6(a) shows the corresponding simulation results in terms of stress–strain hysteresis curves. Because of their characteristic shape, such behavior has been termed *magnetic field (and stress) biased pseudo- or superelasticity*, cf. Straka and Heczko (2003) and Kiefer and Lagoudas (2009). One has to keep in mind, however, that the origin of this effect is not martensitic phase transformation, as in conventional shape memory alloys, but rather stress-induced variant reorientation. The associated evolutions of the volume fractions are shown in Figs. 6(b)–(d). The specific constant values of $\bar{\sigma}_{33}$ and \bar{h}_2 for each considered case are given in the legend of the figure. Curves with the label “Reference” are identical to those previously shown in Figs. 4 and 5.

It is clear from (40) that the strain response ε_{11} is mainly governed by the evolution of martensite volume fractions, particularly that of variant 1. The elastic straining due to $\bar{\sigma}_{11}$, also visible in Fig. 6(a), is essentially negligible and the offset strains occurring during loading stages 1 and 2—partially stemming from elastic contributions as well as the transformations strains due to variant switching—have been eliminated from the response plots. It is observed that while the evolution of ξ_1 is qualitatively similar in each of the four different cases, volume fractions ξ_2 and ξ_3 evolve quite differently. For example, the material is initially comprised entirely of martensite variant 3 in the reference case and for $\bar{\sigma}_{33} = -3.0$ MPa, $\mu_0 \bar{h}_2 = 0.45$ T. For the lower stress level ($\bar{\sigma}_{33} = 0.0$ MPa) and a higher level of the applied magnetic field ($\mu_0 \bar{h}_2 = 0.9$ T), however, the third martensite variant does not occur at all. In these last two cases, the material purely consists of the second variant at the beginning of the third loading stage and stress-induced switching only occurs between variants 1 and 2. In contrast, the loading conditions $\bar{\sigma}_{33} = -3.0$ MPa and $\mu_0 \bar{h}_2 = 0.45$ T prevent the nucleation of variant 2, so that switching only occurs between variants 1 and 3.

It has thus successfully been demonstrated that the fully three-dimensional convexification approach (model II) and its algorithmic implementation (cf. algorithm 2 summarized in Table 3) are able to handle complex and energetically competing switching events between all three variants as well as magnetization vector orientations that are no longer restricted to planar rotations.

6. Summary and Outlook

In this work, an energy-relaxation modeling framework for single-crystalline magnetic shape memory alloys was established that successfully captures various three-dimensional effects. As a first generalization step, a rank-one convexification approach (with respect to first-order laminates), originally designed for two-dimensional problems, was extended by allowing all vector-valued microstructural variables to take on arbitrary orientations in \mathbb{R}^3 . Secondly, an extended convexification-based model was

introduced, that incorporates the third tetragonal variant of $\text{Ni}_2\text{-MnGa}$ (5 M) martensite with all vectorial variables now parameterized in \mathbb{R}^3 . While some aspects of this generalization are straightforward, others are not. The formulation of proper dissipation potential and hardening function expressions, for instance, had to be handled with great care, considering that in the three-variant model there exists more than one (forward/reverse) switching path and that all switching possibilities must, at least in principle, be allowed to happen simultaneously. Another major contribution of this work is the algorithmic treatment of the constitutive equations of this type. In addition to their obvious nonlinearity and coupled multi-field nature, a particular challenge of the relaxation-based models is the need to enforce relatively large sets of equality and particularly inequality constraints during minimization. In previous works, algorithmic formulations based on the elegant complementarity function approach have successfully been used by the authors to handle this difficulty (Kiefer et al., 2012; Buckmann et al., 2019; Bartel et al., 2019; Bartel et al., 2020). Here, however, a novel staggered augmented Lagrangian scheme was formulated and implemented, since it showed greater robustness in dealing with the additional level of complexity associated with the extended formulations. The observed advantages of the augmented Lagrangian formulation were similar to those discussed in the literature on crystal plasticity (Schmidt-Baldassari, 2003; Prueger and Kiefer, 2020) and shape memory alloy modeling (Stupkiewicz and Petryk, 2013).

Two types of numerical experiments were performed to test the generalized relaxation models for MSMA. Firstly, both extended formulations were shown to recover the solution predicted by the two-dimensional model for the special case of transverse magnetic field-induced straining at different axial bias stress levels. This loading case is of particular importance, since it corresponds to the most common testing setup for MSMA single crystals and because the two-dimensional constitutive model described in Section 2 was successfully validated on the basis of such experimental data (Bartel et al., 2020). Secondly, to assess the predictive capabilities and robustness of the extended convexification model, a more complex loading scenario—also motivated by experiments (Feigenbaum et al., 2016)—was considered, in which the evolution of the third variant plays a key role. To correlate the interplay of microstructural mechanisms with the predicted effective sample response, 3D-visualizations were introduced that quantitatively reflect current values of the microstructural variables (domain-variant volume fractions, magnetization vector orientations) at different stages along the loading path. It is found that the proposed modeling framework and solution algorithms are indeed able to successfully describe this much more complicated three-dimensional, three-variant MSMA constitutive response.

All computations in this work—and also the reduced forms in which the model equations were presented—assumed spatial homogeneity of all fields within the sample. The importance of being able to solve inhomogeneous problems, however, immediately becomes apparent for non-simple sample geometries and particularly if one is interested in local quantities, rather than volume averages over the entire specimen (Haldar et al., 2016). To this end, a mixed finite element formulation was recently proposed in Buckmann et al. (2019) that incorporates the described energy relaxation approach to MSMA modeling. The combination of this finite element framework with the models proposed in the current work constitutes future research, for which first steps towards such formulations have been discussed in Bartel et al. (2018). The present modeling framework would generally also be suitable for conventional FEM platforms, provided those offer the possibility of defining user elements (in addition to user material routines).

A remaining challenge for future work is the extension to higher-order laminates—with rank-one compatible interfaces—for the three-dimensional case. Work by Tsou and Huber (Tsou and Huber, 2010) on compatible domain structures in ferroelectric single crystals could potentially serve as inspiration here—although enforcing the compatibility of freely rotating magnetization (or magnetic induction) vectors is expected to be more advanced than for polarizations with fixed spatial orientation. An important step leading in this direction is to incorporate notions analogous to rank-one convexification for the magnetic field variables into the relaxation framework, as recently proposed in Kiefer et al. (2017). Moreover, the fully-three dimensional convexification model introduced in this contribution ought to be implemented into a generalized version of the finite element framework discussed above. This will be necessary to take full advantage of the capabilities of the extended 3D-constitutive model and is expected to lead to a significant further improvement of the quantitative accuracy of the predictions—particularly for the simulation of experimental settings and engineering applications with complex magnetomechanical loading.

Declaration of Competing Interest

The authors declare that they have no known competing financial interests or personal relationships that could have appeared to influence the work reported in this paper.

Acknowledgments

The financial support by the German Research Foundation (DFG) through the Research Unit 1509: “Ferroic Functional Materials: Multi-Scale Modeling and Experimental Characterization”, projects P6 (ME 1745/8-2) and P7 (KI 1392/4-2, BA 4195/2-2), is gratefully acknowledged.

References

- Auricchio, F., Bessoud, A.L., Reali, A., Stefanelli, U., 2015. A phenomenological model for the magneto-mechanical response of single-crystal magnetic shape memory alloys. *Eur. J. Mech. – A/Solids* 52, 1–11.
- Ball, J.M., James, R.D., 1987. Fine phase mixtures as minimizers of energy. *Arch. Ration. Mech. Anal.* 100, 13–52.
- Bartel, T., Guschke, I., Menzel, A., 2019. Towards the simulation of selective laser melting processes via phase transformation models. *Computers Math. Appl.* 78, 2267–2281.
- Bartel, T., Hackl, K., 2009. A micromechanical model for martensitic phase-transformations in shape-memory alloys based on energy-relaxation. *Zeitschrift für Angewandte Mathematik und Mechanik* 89, 792–809.
- Bartel, T., Kiefer, B., Buckmann, K., Menzel, A., 2015. A kinematically-enhanced relaxation scheme for the modeling of displacive phase transformations. *J. Intell. Mater. Syst. Struct.* 26, 701–717.
- Bartel, T., Kiefer, B., Buckmann, K., Menzel, A., 2018. A finite-element framework for the modelling and simulation of phase transforming magnetic solids using energy relaxation concepts. *Proc. Appl. Math. Mech.* 18, e201800415.
- Bartel, T., Kiefer, B., Buckmann, K., Menzel, A., 2020. An energy-relaxation-based framework for the modelling of magnetic shape memory alloys – simulation of key response features under homogeneous loading conditions. *Int. J. Solids Struct.* 182–183, 162–178.
- Bartel, T., Menzel, A., Svendsen, B., 2011. Thermodynamic and relaxation-based modeling of the interaction between martensitic phase transformations and plasticity. *J. Mech. Phys. Solids* 59, 1004–1019.
- Bartel, T., Schulte, R., Menzel, A., Kiefer, B., Svendsen, B., 2019. Investigations on enhanced Fischer-Burmeister NCP functions: Application to a rate-dependent model for ferroelectrics. *Arch. Appl. Mech.* 89, 995–1010.
- Bertsekas, D.P., 1982. *Constrained Optimization and Lagrange Multiplier Methods*. Academic Press, New York.
- Biot, M.A., 1965. *Mechanics of Incremental Deformations*. Wiley, New York.
- Brown, Jr., W.F., 1963. *Micromagnetics*. volume 18 of *Interscience Tracts on Physics and Astronomy*. John Wiley & Sons, New York.
- Brown, Jr., W.F., 1966. *Magnetoelastic Interactions*. volume 9 of *Tracts in Natural Philosophy*. Springer-Verlag, New York.
- Buckmann, K., Kiefer, B., Bartel, T., Menzel, A., 2019. Simulation of magnetised microstructure evolution based on a micromagnetics-inspired FE framework:

- Application to magnetic shape memory behaviour. *Arch. Appl. Mech.* 89, 1085–1102.
- Chen, X., Mouni, Z., He, Y., Zhang, W., 2014. A three-dimensional model of magneto-mechanical behaviors of martensite reorientation in ferromagnetic shape memory alloys. *J. Mech. Phys. Solids* 64, 249–286.
- Dacorogna, B., 1982. Quasiconvexity and relaxation of the nonconvex problems in the calculus of variations. *J. Funct. Anal.* 46, 102–118.
- Dai, L., Cullen, J., Wuttig, M., 2004. Intermartensitic transformation in a NiMnGa alloy. *J. Appl. Phys.* 95, 6957–6959.
- DeSimone, A., 2004. Coarse-grained models of materials with non-convex free-energy: Two case studies. *Comput. Methods Appl. Mech. Eng.* 193, 5129–5141.
- DeSimone, A., James, R.D., 2002. A constrained theory of magnetoelasticity. *J. Mech. Phys. Solids* 50, 283–320.
- DeSimone, A., Kohn, R.V., Müller, S., Otto, F., 2006. Recent analytical developments in micromagnetics. In: Bertotti, G., Mayergoyz, I. (Eds.), *The Science of Hysteresis, Volume II: Physical modeling, micromagnetics, and magnetization dynamics*, chapter 4. Elsevier, Amsterdam, pp. 269–381.
- Feigenbaum, H.P., Ciocanel, C., Eberle, J.L., Dikes, J.L., 2016. Experimental characterization and modeling of a three-variant magnetic shape memory alloy. *Smart Mater. Struct.* 25, 104004.
- Gauthier, J.Y., Lexcellant, C., Hubert, A., Abadie, J., Chaillet, N., 2011. Magneto-thermo-mechanical modeling of a magnetic shape memory alloy Ni–Mn–Ga single crystal. *Ann. Solid Struct. Mech.* 2, 19–31.
- Haldar, K., Kiefer, B., Lagoudas, D.C., 2011. Finite element analysis of the demagnetization effect and stress inhomogeneities in magnetic shape memory alloy samples. *Phil. Mag.* 91, 4126–4157.
- Haldar, K., Kiefer, B., Menzel, A., 2016. Finite element simulation of rate-dependent magneto-active polymer response. *Smart Mater. Struct.* 25, 104003.
- Halphen, B., Nguyen, Q.S., 1975. Sur les matériaux standards généralisés. *J. de Mécanique* 14, 39–63.
- Heczko, O., 2005. Magnetic shape memory effect and magnetization reversal. *J. Magn. Magn. Mater.* 290–291, 787–794.
- Heczko, O., Sozinov, A., Ullakko, K., 2000. Giant field-induced reversible strain in magnetic shape memory NiMnGa alloy. *IEEE Trans. Magn.* 36, 3266–3268.
- Heczko, O., Straka, L., Ullakko, K., 2003. Relation between structure, magnetization process and magnetic shape memory effect of various martensites occurring in Ni–Mn–Ga alloys. *J. Phys. IV* 112, 959–962.
- Junker, P., Hackl, K., 2011. Finite element simulations of polycrystalline shape memory alloys based on a micromechanical model. *Comput. Mech.* 47, 505–517.
- Kiang, J., Tong, L., 2005. Modelling of magneto-mechanical behaviour of Ni–Mn–Ga single crystals. *J. Magn. Magn. Mater.* 292, 394–412.
- Kiang, J., Tong, L., 2007. Three-dimensional constitutive equations for Ni–Mn–Ga single crystals. *J. Magn. Magn. Mater.* 313, 214–229.
- Kiefer, B., Bartel, T., 2017. On variationally-consistent homogenization approaches in multi-phase magnetic solids. *Proc. Appl. Math. Mech.* 17, 517–518.
- Kiefer, B., Bartel, T., Menzel, A., 2012. Implementation of numerical integration schemes for the simulation of magnetic sma constitutive response. *Smart Mater. Struct.* 21, 094007.
- Kiefer, B., Buckmann, K., Bartel, T., 2015. Numerical energy relaxation to model microstructure evolution in functional magnetic materials. *GAMM-Mitteilungen* 38, 171–196.
- Kiefer, B., Furlan, T., Mosler, J., 2017. A numerical convergence study regarding homogenization assumptions in phase field modeling. *Int. J. Numer. Meth. Eng.* 112, 1097–1128.
- Kiefer, B., Karaca, H.E., Lagoudas, D.C., Karaman, I., 2007. Characterization and modeling of the magnetic field-induced strain and work output in Ni₂MnGa shape memory alloys. *J. Magn. Magn. Mater.* 312, 164–175.
- Kiefer, B., Lagoudas, D.C., 2005. Magnetic field-induced martensitic variant reorientation in magnetic shape memory alloys. *Phil. Magazine Special Issue: Recent Adv. Theor. Mech.* 85, 4289–4329.
- Kiefer, B., Lagoudas, D.C., 2008. Modeling of magnetic SMAs. In: Lagoudas, D.C. (Ed.), *Shape Memory Alloys: Modeling and Engineering Applications*. Springer-Verlag, New York, pp. 325–393.
- Kiefer, B., Lagoudas, D.C., 2009. Modeling the coupled strain and magnetization response of magnetic shape memory alloys under magnetomechanical loading. *J. Intell. Mater. Syst. Struct.* 20, 143–170.
- Lagoudas, D.C. (Ed.), 2008. *Shape Memory Alloys: Modeling and Engineering Applications*. Springer-Verlag, New York.
- LaMaster, D.H., Feigenbaum, H.P., Ciocanel, C., Nelson, I.D., 2015. A full 3d thermodynamic-based model for magnetic shape memory alloys. *J. Intell. Mater. Syst. Struct.* 26, 663–679.
- Li, J.Y., Ma, Y.F., 2008. Magnetoelastic modeling of magnetization rotation and variant rearrangement in ferromagnetic shape memory alloys. *Mech. Mater.* 40, 1022–1036.
- Ma, Y.F., Li, J.Y., 2007. Magnetization rotation and rearrangement of martensite variants in ferromagnetic shape memory alloys. *Applied Physics Letters* 90, 172504–1–3.
- Miehe, C., Rosato, D., Kiefer, B., 2011. Variational principles in dissipative electro-magneto-mechanics: A framework for the macro-modeling of functional materials. *Int. J. Numer. Meth. Eng.* 86, 1225–1276.
- Morrey, C.B., 1952. Quasi-convexity and the lower semicontinuity of multiple integrals. *Pac. J. Math.* 2, 25–53.
- O’Handley, R.C., 2000. *Modern Magnetic Materials*. John Wiley & Sons, New York.
- Ozdemir Kart, S., Cagin, T., 2010. Elastic properties of Ni₂MnGa from first-principles calculations. *J. Alloy. Compd.* 508, 177–183.
- Prueger, S., Kiefer, B., 2020. A comparative study of integration algorithms for finite single crystal (visco-)plasticity. *Int. J. Mech. Sci.* 180, 105740.
- Schmidt-Baldassari, M., 2003. Numerical concepts for rate-independent single crystal plasticity. *Comput. Methods Appl. Mech. Eng.* 192, 1261–1280.
- Sedláč, P., Seiner, H., Bodnárová, L., Heczko, O., Landa, M., 2017. Elastic constants of non-modulated Ni–Mn–Ga martensite. *Scripta Mater.* 136, 20–23.
- Straka, L., 2007. Magnetic and magneto-mechanical properties of Ni–Mn–Ga magnetic shape memory alloys Ph.D. dissertation. Helsinki University of Technology.
- Straka, L., Heczko, O., 2003. Superelastic response of Ni–Mn–Ga martensite in magnetic fields and a simple model. *IEEE Trans. Magn.* 39, 3402–3404.
- Straka, L., Heczko, O., Novak, V., Lanska, N., 2003. Study of austenite-martensite transformation in Ni–Mn–Ga magnetic shape memory alloy. *J. Phys. IV* 112, 911–915.
- Stupkiewicz, S., Petryk, H., 2013. A robust model of pseudoelasticity in shape memory alloys. *Int. J. Numer. Meth. Eng.* 93, 747–769.
- Tickle, R., James, R.D., Shield, T., Wuttig, M., Kokorin, V.V., 1999. Ferromagnetic shape memory in the NiMnGa system. *IEEE Trans. Magn.* 35, 4301–4310.
- Tsou, N.T., Huber, J.E., 2010. Compatible domain structures and the poling of single crystal ferroelectrics. *Mech. Mater.* 42 (42), 740–753.